

Strong asymptotic giant branch stars' spectral features in distant quiescent galaxies: Impact on galaxy evolution

Shiying Lu^{1,2,3}, Emanuele Daddi², Claudia Maraston⁴, Mark Dickinson⁵, Pablo Arrabal Haro⁵, Raphael Gobat⁶, Alvio Renzini⁷, Mauro Giavalisco⁸, Micaela B. Bagley⁹, Antonello Calabrò¹⁰, Yingjie Cheng⁸, Alexander de la Vega¹¹, Chiara D'Eugenio^{12,14}, David Elbaz², Steven L. Finkelstein⁹, Carlos Gómez-Guijarro², Qiusheng Gu^{1,3}, Nimish P. Hathi¹³, Marc Huertas-Company^{12,14,15}, Jeyhan S. Kartaltepe¹⁶, Anton M. Koekemoer¹³, Aurélien Le Bail¹⁷, Yipeng Lyu², Benjamin Magnelli², Bahram Mobasher¹¹, Casey Papovich^{18,19}, Nor Pirzkal²⁰, R. Michael Rich²¹, Sandro Tacchella^{22,23} and L. Y. Aaron Yung¹³

¹School of Astronomy and Space Science, Nanjing University, Nanjing, 210093, China

²Université Paris-Saclay, Université Paris Cité, CEA, CNRS, AIM, Paris, 91191, France

³Key Laboratory of Modern Astronomy and Astrophysics (Nanjing University), Ministry of Education, Nanjing, 210093, China

⁴Institute of Cosmology and Gravitation, University of Portsmouth, Dennis Sciama Building, Burnaby Road, Portsmouth PO1 3FX, UK

⁵NSF's National Optical-Infrared Astronomy Research Laboratory, 950 N. Cherry Ave. Tucson, AZ 85719, USA

⁶Instituto de Física, Pontificia Universidad Católica de Valparaíso, Casilla 4059, Valparaíso, Chile

⁷INAF-Osservatorio Astronomico di Padova, Vicolo dell'Osservatorio 5, I-35122 Padova, Italy

⁸University of Massachusetts Amherst, 710 North Pleasant Street, Amherst, MA 01003-9305, USA

⁹Department of Astronomy, The University of Texas at Austin, Austin, TX, USA

¹⁰INAF-Osservatorio Astronomico di Roma, via di Frascati 33, 00078 Monte Porzio Catone, Italy

¹¹Department of Physics and Astronomy, University of California, 900 University Ave, Riverside, CA 92521, USA

¹²Instituto de Astrofísica de Canarias (IAC), 38205 La Laguna, Tenerife, Spain

¹³Space Telescope Science Institute, 3700 San Martin Dr., Baltimore, MD 21218, USA

¹⁴Universidad de la Laguna, La Laguna, Tenerife, Spain

¹⁵Université Paris-Cité, LERMA - Observatoire de Paris, PSL, Paris, France

¹⁶Laboratory for Multiwavelength Astrophysics, School of Physics and Astronomy, Rochester Institute of Technology, 84 Lomb Memorial Drive, Rochester, NY 14623, USA

¹⁷Department of Physics, University of California Merced, 5200 Lake Road, Merced, CA 95343, USA

¹⁸Department of Physics and Astronomy, Texas A&M University, College Station, TX, 77843-4242, USA

¹⁹George P. and Cynthia Woods Mitchell Institute for Fundamental Physics and Astronomy, Texas A&M University, College Station, TX, 77843-4242, USA

²⁰ESA/AURA Space Telescope Science Institute

²¹Department of Physics and Astronomy, University of California,

Los Angeles, CA, 90095, USA

²²Kavli Institute for Cosmology, University of Cambridge, Madingley Road, Cambridge, CB3 0HA, UK

²³Cavendish Laboratory, University of Cambridge, 19 JJ Thomson Avenue, Cambridge, CB3 0HE, UK

Age-dating and weighting stellar populations in galaxies at various cosmic epochs are essential steps to study galaxy formation through cosmic times. Evolutionary population synthesis models with different input physics are used towards this aim. In particular, the contribution from the thermally pulsing asymptotic-giant-branch (TP-AGB) stellar phase, which peaks for intermediate-age 0.6–2 Gyr systems, has been debated upon for decades. Here we report the detection of strong cool star signatures in the rest-frame near-infrared spectra of three young (~ 1 Gyr), massive ($\sim 10^{10} M_{\odot}$) quiescent galaxies at large look-back time, $z=1-2$, using JWST/NIRSpec. The co-existence of oxygen- and carbon-type absorption features, spectral edges and features from rare species such as Vanadium, and possibly Zirconium, reveal a strong contribution from TP-AGB stars. Population synthesis models with significant TP-AGB contribution reproduce the observations considerably better than those with weak TP-AGB, which are those commonly used. These findings call for revisions of published stellar population fitting results, pointing to lower masses and younger ages, with additional implications on cosmic dust production and chemical enrichment. These results will stimulate new generations of improved models informed by these and future observations.

1 Introduction

The TP-AGB – an advanced evolutionary stage of intermediate-mass stars ($\sim 1-10 M_{\odot}$) – is a potentially essential component of stellar population models. The study of the TP-AGB contribution to the light of stellar population has a long history. The first estimate goes back over 30 years¹ and was based on the *fuel consumption theorem*, thus predicting that the TP-AGB contribution to the bolometric light of a simple stellar population (SSP) could approach or

even exceed $\sim 50\%$ at intermediate ages from ~ 40 Myr to a few Gyr. Subsequent models estimated a contribution to up to $\sim 80\%$ of the integrated near-infrared (NIR) emission of stellar populations with ages in the range of $0.2 \lesssim t \lesssim 2$ Gyr ²⁻⁶.

However, the actual energetic contribution and spectral composition of this phase are highly controversial, with different models adopting distinctively different prescriptions for both the energetics and the stellar spectra during this phase ^{3,7-9}. These uncertainties stem from two complications typical of the TP-AGB phase, namely its double-shell burning regime leading to instabilities and ‘thermal pulses’ occurring on short timescales alongside a strong mass-loss, both requiring calibration of free parameters such as convection, mixing and mass loss with observational data ^{10,11}. As a consequence, stellar evolutionary computations, which are the backbone of evolutionary population synthesis models, typically terminate at the end of the Early Asymptotic Giant Branch (E-AGB) phase, and the inclusion of the TP-AGB in integrated models is performed separately either using specific TP-AGB tracks ^{4,8} or fuel-consumption-theorem estimated TP-AGB energetics ³.

Historically, the early Maraston models (i.e. M05 ³) based on the *fuel consumption theorem* ¹² pioneered the incorporation of the TP-AGB phase into population synthesis models by calibrating the energetics of TP-AGB tracks with observed photometric data and adopting observed oxygen-rich (O-rich) and carbon-rich (C-rich) spectra ^{13,14}. These M05 models, forecasting the onset of the TP-AGB phase as a sharp transition (e.g., a rapid increase in the TP-AGB bolometric and near-IR contribution to the energetics of stellar populations, see Figure 3 in Ref. ²) around 0.2 Gyr and lasting up to 2 Gyr, are referred to as “TP-AGB-heavy”. A similar modelling approach is found in the Conroy models (i.e., C09 ⁹), but with two modifications, namely a substantial reduction of the energetics and a shift towards older ages (1-3 Gyr) for the relevant population epoch, which dilute the TP-AGB ‘phase transition’. Therefore, the C09 models are referred to as “TP-AGB-light”. Following the availability of new data for the calibration and adopting some of the C09 arguments, the calibration of the TP-AGB contribution as a function of age was revised using Magellanic Clouds globular clusters data ¹⁰, based on which an update of the M05 models was presented (so-called M13). The M13 models have a reduced TP-AGB fuel consumption and a slightly older onset age (600 Myr) with respect to M05, but they still forecast a sharp transition for the TP-AGB onset and a sizable fuel consumption. The M13 models are referred to as “TP-AGB-mild”. On a different route, the widely used Bruzual & Charlot models (i.e., BC03 ⁷), based on *isochrone synthesis* of stellar evolutionary tracks ¹⁵, adopt different energetics and spectra for the TP-AGB phase. Since this results in a negligible TP-AGB contribution to the integrated spec-

trum, the BC03 models are referred to as “TP-AGB-poor”.

A number of studies have attempted to observationally constrain the contribution of the TP-AGB phase by fitting spectra and photometric spectral energy distributions (SEDs) of different kinds of galaxies (post-starbursts, Seyferts, spirals, and passive) over a range of redshifts, but with conflicting results ¹⁶⁻²¹. It was early suggested (M05) that high-redshift galaxies with low star formation (‘quiescent’) are the ideal laboratories for this test, as their mass-weighted ages (~ 1 Gyr) correspond to the expected maximum possible contribution of the TP-AGB stars to the rest-frame NIR spectrum of such galaxies. High quality observations of NIR galaxy spectra dominated by TP-AGB stars are still missing: ground-based spectra below $2.3\mu\text{m}$ are impacted by atmospheric emission and absorption, and HST NIR grism spectra lack sufficient sensitivity. The JWST has now the wavelength coverage and sensitivity to finally settle this issue.

2 Results

Selection of quiescent candidates

We selected 1084 quiescent galaxy candidates at $z_{\text{phot}} > 1$ using a catalog ²² in the EGS CANDELS field ^{23,24}, based on the UVJ diagram ²⁵ and SED modeling (adopting exponentially declining star formation history, namely $\text{SFH} \sim e^{-t/\tau}$ and requiring $t/\tau > 1.0$). The $z > 1$ limit imposed on the sample ensures that the age-sensitive spectral region around rest-frame 4000Å break is covered by JWST/NIRSpec with good sensitivity. We cross-matched these photometrically-selected candidates with the 1491 galaxies with secure spectroscopic redshift observed with JWST/NIRSpec during the Cosmic Evolution Early Release Science (CEERS) program ^{26,27} and during a subsequent NIRSpec follow-up program (DD-2750) ²⁸. This resulted in a spectroscopic sample of 31 galaxies, for which we visually inspected the spectra. Some spectra have low signal-to-noise ratios (SNR) because the galaxies are too faint or were poorly centered in the NIRSpec’s micro-shutter apertures. Other spectra exhibit strong emission lines consistent with either active star formation or an active galactic nucleus (AGN), or that have redshifts that are too high ($z > 3$) to provide adequate coverage of the relevant rest-frame NIR wavelengths. We retained three galaxies, IDs = 8595, 9025, and D36123 with redshifts at $1 < z < 2$, whose spectra clearly show the D4000 break, no obvious emission lines, and also have relatively high signal-to-noise ratio (SNR). This is a small yet representative sample fulfilling these criteria.

The spectrum of D36123

Galaxy D36123, the primary target in this work, exhibits an exceptionally high-quality PRISM spectrum with an average of $\text{SNR} \gtrsim 187$ per spectral pixel (Fig.1; plotted as a double histogram to show the $\pm 1\sigma$ noise). Its relatively bright

flux ($\text{mag}_{\text{AB}}=21.4$ at $3.6\mu\text{m}$), steep radial surface brightness profile (Sérsic $n \sim 4$, see Table 3), longer exposure time and accurate centering into the micro-shutters, which minimizes the effect of path loss and aperture correction (see Methods), are the reasons for the remarkable quality of this spectrum.

A large number of features are clearly detected at rest-frame wavelengths from 0.3 to $2.0\mu\text{m}$, for which we propose identifications (see labels in Fig.1). Besides common absorption features at $\lambda_{\text{rest}} < 5500\text{\AA}$ typical of quiescent galaxies, such as Ca H+K, H δ , H γ +G4300 and absorption from heavy elements (such as Mg, Ca, and Fe), which have been observed in quiescent galaxies’ spectra at high redshift²⁹, the rest-frame NIR spectrum exhibits numerous absorption features and band edges. The relatively low spectral resolution ($R \sim 30\text{--}300$) of the NIRSpec PRISM helps in the detection of these broad features. The proposed identifications are obtained by comparing our spectrum with empirical libraries of C-rich¹⁴ and O-rich¹³ TP-AGB stars (see Fig.2). These observed spectral features are related to diverse stellar types in the AGB phase, i.e. E-AGB and TP-AGB^{30–33}. The deep CN edges in Fig.2a (most striking is the CN1.1 μm edge, see Fig.1, where the continuum suddenly drops down by $\sim 15\%$ in the observed spectrum) are particularly enhanced in rich N-type carbon stars^{30–32}, that are produced by the third dredge-up and therefore demonstrate the presence of a contribution by TP-AGB stars. On the other hand, the TiO and VO absorption bands (see Fig.2b) are produced in the spectra of M-type stars in either the RGB or AGB phases³¹. However, the best-fit spectrum of BC03 models, that includes only the RGB contribution, is almost featureless in the NIR (Fig. 3) and we conclude that also the oxygen-rich features in the spectrum of D36123 are due to TP-AGB stars. This is the first time that multiple TiO absorptions concomitant with CN and C₂ features are identified in an observed galaxy spectrum, pointing to the simultaneous presence of O-rich and C-rich cool stars. This is naturally expected in presence of a broad distribution of stellar metallicities, which must exist in massive galaxies, such that the metal-poor stars evolve preferentially into carbon-rich TP-AGB stars, and the metal-rich ones into oxygen-rich (M Type) TP-AGB stars. Since V and Zr are only produced by *s*-process nucleosynthesis, those VO and ZrO features (see Fig.2b) are expected to be detectable only in the coolest TP-AGB stars^{31,33}, demonstrating the prominence of the TP-AGB phase in the light emitted by this $z \sim 1$ quiescent galaxy. Note also the broad depressions due to water, again indicating the presence of O-rich M-type stars.

We then performed spectral fitting on the observed spectrum of D36123, employing four models – BC03, C09, M13, and M05 (spanning the full range from TP-AGB poor to heavy, see Fig.3 and Table 1). We used delayed exponentially declining SFH $\sim (t/\tau^2)e^{-t/\tau}$ with a large variety of timescales and stellar ages, interpolated over a grid of metal-

licities, and allowed for dust extinction. In convolving the models to match the resolution of observed spectra, we considered the instrumental resolution, the wavelength sampling of the spectral template models, and the estimated stellar velocity dispersion of the galaxy (see Methods). We find that our model fitting results are robust against (1) more complex star-formation histories allowing for bursts and sudden truncations; (2) linear combinations of models with different ages and metallicities (which is equivalent to non-parametric SFH); (3) alternative attenuation curves or without considering the reddening by dust; (4) variations to the aperture correction recipe; (5) modifications of the spectral extraction apertures over 3 or 5 pixels; (6) modelling of emission lines. The minimum reduced χ^2 from each model is barely affected when these variations are considered.

The “TP-AGB-mild/heavy” (i.e., M13 and M05) models can produce the largest fraction of the detected features, while the “TP-AGB-poor/light” predict much weaker spectral features in the NIR, as Fig.3 illustrates. Among the four models, the TP-AGB-mild model, M13, provides by far the best fit. Additionally, M13 also identifies the majority of TP-AGB features (i.e., four TiO absorptions and most CN edges). However, there are strong spectral features that are clearly not present (or much weaker than in the observed spectrum) even in the M13 best-fit spectrum, like several TiO and C₂ absorptions. The strong CN1.1 μm spectral edge is only present in the M13/M05 models. Interestingly, the MgII-band at $0.52\mu\text{m}$, part of Lick set of indexes³⁴ is much weaker in all models than in the data, pointing to a strong contribution from TiO bands all the way to $0.5\mu\text{m}$, as expected for M-type stars (and, possibly, to $[\alpha/\text{Fe}]$ -enhancement³⁵). The M05 shows the worst overall fit due to clear discrepancy at $\lambda_{\text{rest}} < 5000\text{\AA}$ (see Fig.10 in Methods), but still displays significantly more numerous matching TP-AGB features in the NIR than the C09 and BC03 models (see Fig.3), noticeably the long-sought C₂ absorption around $1.75\mu\text{m}$. Moreover, when fitting the spectrum over the restricted rest-frame wavelength range $< 5000\text{\AA}$ all models converge to a mass-weighted age of about 1 Gyr, which is indeed the age where TP-AGB features are expected to be at peak^{3,10}. Therefore, we can conclude that it is the treatment of the TP-AGB in the models that most affects the goodness of fit in our $z \sim 1$ quiescent galaxies. Even for the best-fit model M13, the minimum reduced $\chi^2_R \sim 39$ is large, indicating that also this model is lacking some stellar ingredients that are present in the galaxy, and are needed.

Some of the observed features are also found in the coolest phase of (M-type) red-giant-branch (RGB) stars and in the red-supergiant (RSG) phase of massive stars, with ages around 10 Myr^{13,30,33}. We could safely exclude that RSG stars contribute substantially due to the inferred mass-weighted age (~ 1 Gyr) and negligible residual star forma-

tion rate, when fitting only the optical spectrum (see Table 1). This is suggestive of a negligible contribution from short-lived massive stars. Instead, M-type RGB stars certainly contribute to the NIR spectrum at these ages, to a degree that is, however, model-dependant because the onset and development of the RGB phase depends on the overshooting assumed in stellar tracks^{3,36}. The full RGB contribution to the total light in the K-band around 1 Gyr is $\sim 20 - 30\%$ according to M05 models and $\sim 10 - 20\%$ for BC03-type models and the upper part of the RGB where M-giants form is a further fraction of this. Therefore, while contributing, M-type RGB stars do not dominate the spectrum. We verified this point by comparing our observed spectrum to a further stellar population model including empirical spectra for the RGB (and other phases; E-MILES³⁷), but not including a treatment of the TP-AGB phase. This model cannot reproduce more features than the BC03/C09 models.

The best-fitting physical parameters presented in Table 1 exemplify the impact of the chosen model on the derived properties. For instance, comparing results between BC03 and M13 in the full rest-frame spectral range, there is only 30% discrepancy in stellar mass, but the impact on ages is strong with $\Delta t \sim 1$ Gyr (the M13 age is almost three times lower than the BC03 age – all reported age measurements in this work are mass-weighted), despite the higher metallicity preferred by the BC03 fit. These age differences affect the derived formation epochs and evolutionary timescales of galaxies. The BC03 best-fit age of 1.7 Gyr is consistent with a RGB contribution of about 20% for those models (see Figure 2 in Ref.³⁸), which likely contributes to some of the observed features and NIR flux. However, this fitted age is still too young for the contribution from red giant stars to be dominant, further supporting the arguments described above.

The spectra of galaxies 8595 and 9025

The spectra of the other two fainter quiescent galaxies, 8595 ($\text{mag}_{\text{AB}}=24$ at $3.6\mu\text{m}$, observed with the PRISM) and 9025 ($\text{mag}_{\text{AB}}=23$ at $3.6\mu\text{m}$, observed with the medium-resolution gratings but rebinned to the PRISM resolution), have substantially lower SNR of ~ 15 and 7. Nevertheless, the SNR is still sufficient for the direct detection of individual absorption features in object 8595 (Fig.4), some of the strongest also observed in object 9025 (Fig.5). This includes some TiO absorptions and CN spectral edges, and tentatively a C₂ absorption.

Table 2 presents the results of the best spectral fits of objects 8595 and 9025, based on the different models. For object 8595, we carefully account for a neighbouring bright galaxy when measuring its photometry to estimate spectral aperture corrections, following a similar approach to what is done for object D36123 (see Methods). Again, M13 yields the best-fit spectral fits for both galaxies, with $\chi_R^2 \sim 0.8$ for

object 8595, and $\chi_R^2 \sim 1.7$ for object 9025. The derived stellar masses differ at most by 0.16 dex between the M13 and BC03 models, but the best-fit ages are even more strongly dependent on the specific model used (stellar age differences from 0.1 to 1 Gyr). In Table 2, the values $\Delta\chi^2$ denote the χ^2 difference with respect to the M13 model. The small cumulative probability $P(\Delta\chi^2)$ suggests the preference for the M13 model is statistically significant at the ($> 99.9\%$ confidence level) in the overall spectral fit for these two galaxies.

3 Discussion

Overall, we conclude that the spectra of distant quiescent galaxies in this study show clear evidence for a substantial contribution of TP-AGB stars of both C and M type, at variance with what predicted by TP-AGB-poor and -light models. The models with significant TP-AGB contribution, such as M13 or M05, are in better agreement with the NIR features in the spectra of these high-redshift quiescent galaxies, and TP-AGB-mild models (i.e., M13) can fit their entire spectra better. These support our conclusion that the TP-AGB is the primary model ingredient driving the fitting of our spectrum.

Previous work¹⁸ based on high-quality NIR spectra of local spiral/Seyfert galaxies reached similar conclusions, favouring M05 models over BC03 models because of the TP-AGB component. Those local spectra cover a wide wavelength range similar to our high-redshift data and display a variety of features, several of which can only be attributed to TP-AGB stars. Previously, a detection of the CN $1.1\mu\text{m}$ band in the NIR spectra of local AGNs was interpreted as a signature of intermediate age populations evolving along the TP-AGB phase³². Although these local observations are remarkable, JWST spectroscopy can directly observe massive, high-redshift galaxies, with low spread in stellar generations, for their stars to evolve to the TP-AGB phase in sync at ages ~ 1 Gyr when the TP-AGB energetic contribution is maximum^{3,5}. This maximizes the contribution of the short TP-AGB phase (~ 3 Myr for an individual star) to the integrated galaxy SED, with respect to systems with ongoing star formation and a lower mass fraction of stars in the appropriate age range. The dominance of the TP-AGB phase also implies that the NIR spectrum will display all its complexity and thus the SED fit becomes challenging.

Indeed, we find that even for the best performing M13 model the χ_R^2 is large for the high SNR spectrum of D36123 that shows stronger absorption features than the model. By separating optical ($\lambda_{\text{rest}} < 0.5\mu\text{m}$) and NIR ($\lambda_{\text{rest}} > 0.5\mu\text{m}$), we confirmed that it is the fit in the NIR spectrum leading to high values of χ^2 , since we find a minimum reduced $\chi_R^2 \sim 9-11$ in the optical spectrum for the four different models (C09 performing best in this case), while all

reduced χ_R^2 values remain large ($\chi_R^2 \sim 40\text{--}60$) when fitting only the NIR spectrum (see Table 1). More in detail, it appears that the rest-frame $0.5 - 1.0\mu\text{m}$ range, where the strongest TiO features are present, is the most problematic region (see Table 1 and Fig.11 in the Methods) since when we exclude this range, both optical and NIR can be fitted to better than 2% accuracy by the M13 model (Fig.11; but not as well by BC03 and CO09).

Several model ingredients could be responsible for this discrepancy. First of all, M13 and M05 use empirical spectra for just the TP-AGB phase. For the other phase that strongly contribute to the NIR, the RGB, classical Kurucz-type theoretical spectra from model atmospheres are adopted, which - as it is well known - do not adequately match all NIR absorption features^{39,40}. Similarly, models based on the empirical RGB spectra perform better, but not for all features³⁹. Notably, studies by different researchers show that all CO NIR spectral features from H to K in local massive early-type galaxies, whose NIR spectrum is dominated by RGB stars, are systematically stronger than those in the models based on empirical libraries⁴¹. This is also supported by the analysis of observed NIR spectra from local spirals and star-forming galaxies⁴². All this suggests that D36123 contain also stars that are more metal rich than those included in the model.

Our model comparison suggests that extensions to the best-fitting models are needed to improve the match to massive galaxy spectra. The M13 models adopt local samples of C-rich and O-rich spectra, which may not cover the range of metallicity and abundance ratios hosted in distant massive ellipticals. The metallicity dependence in M13 models is included using a theoretical prescription¹², by which more metal-rich models have more fuel consumption in O-rich rather than in C-rich phases, but still using the same observed spectra. In particular, M13 models do not treat the relative contributions of C-rich and O-rich TP-AGB stars as a free parameter. Moreover, the calibration of stellar population models requires samples of stellar generations that are as simple as possible, i.e., star clusters, with available independent age and chemical composition from Color Magnitude Diagram (CMD) fitting and stellar spectroscopy. For the TP-AGB phase these calibrating clusters also need to span a wide age range, extending down to ~ 100 Myr. Star clusters with these properties exist in the Magellanic Clouds and have traditionally served to calibrate stellar population models^{2,10,43}. The limitation is that these clusters have sub-solar metallicity and possibly solar or sub-solar element ratios.

Another issue is a galaxy specific chemical pattern. It is well-known that massive galaxies, both locally^{35,44} as well as at high redshift^{29,45,46}, feature $[\alpha/\text{Fe}]$ -enhanced stellar populations. The same galaxies are also found to host en-

hanced ratios of $[\text{C}/\text{Fe}]$ and $[\text{N}/\text{Fe}]$ ^{47,48} and possibly also in Na^{46,49,50}. Empirical libraries based on local, solar-scaled RGB spectra, and the population models based on them, may not reflect these chemical patterns, causing discrepancies. This would mirror a long-standing discrepancy between optical spectral features of massive galaxies and early population models⁵¹, which was solved by $[\alpha/\text{Fe}]$ -enhanced population models⁵². Galaxy spectra like those we present here, with young ages and super-solar metallicity, and possibly various non-solar element enhancements, are unique, with no known counterpart in the local universe. They challenge the models, but also offer the invaluable opportunity to calibrate them, with far-reaching benefit also for stellar evolution and model atmosphere theories.

Astronomers depend on evolutionary population synthesis models to infer the timeline of galaxy formation and evolution. In turn, the model age scale depends on the input stellar evolution in terms of stellar tracks (and their input) and the energetics of stellar phases. We derive systematically younger ages and lower masses when fitting these spectra with TP-AGB-mild models (i.e., M13) versus TP-AGB-poor/-light models (i.e., BC03/CO09), especially at high redshift. The age differences range from ~ 100 Myr to ~ 1 Gyr (see Tables 1 and 2). Younger galaxy ages can have implications for the inferred physics of galaxy evolution, such as gas accretion and star formation quenching. Also galaxy simulations adopt evolutionary population synthesis models as input, hence our results have an impact on the predicted spectra and photometry of simulated galaxies found in cosmological and other simulations⁶. In that case, the age is fixed within the simulation, but the simulated galaxy SEDs and the calibrations through comparisons to observations are obviously affected. The AGB stellar phase has also a major impact on galaxies dust production and chemical evolution particularly for heavy elements⁵³. A higher fuel for this phase, as supported by our findings, has implications on guiding the relevant calculations for these processes⁵⁴, thus potentially having an even broader impact on galaxy evolution.

The spectra presented here demonstrate the presence of TP-AGB spectral features, including those from carbon stars, in the integrated NIR light from high-redshift, quiescent galaxies. These features are first seen in their richness in galaxy spectra. Clearly, our very small galaxy sample does not allow us to infer the statistical impact of the TP-AGB emission on the derived stellar population properties for young quiescent galaxies in general. Previous photometric studies^{5,19} have shown that, on average, fitting distant galaxies using models with heavier TP-AGB contributions yields younger ages and lower stellar masses than TP-AGB-poor models, but also with significant galaxy-by-galaxy differences. The usual degeneracies between age, reddening and metallicity still apply to some extent, and for individual galaxies, the SED fitting results can depend on unknown de-

tails of the past star formation histories (for example). From our small sample, it is also difficult to evaluate how frequently these TP-AGB features are present in early galaxy spectra. NIRSPEC observations for a larger, homogeneously selected sample of galaxies can address these questions and help us to quantify the broader consequences of TP-AGB emission for determining galaxy physical parameters. Such observations may also help guide further improvement of stellar population models.

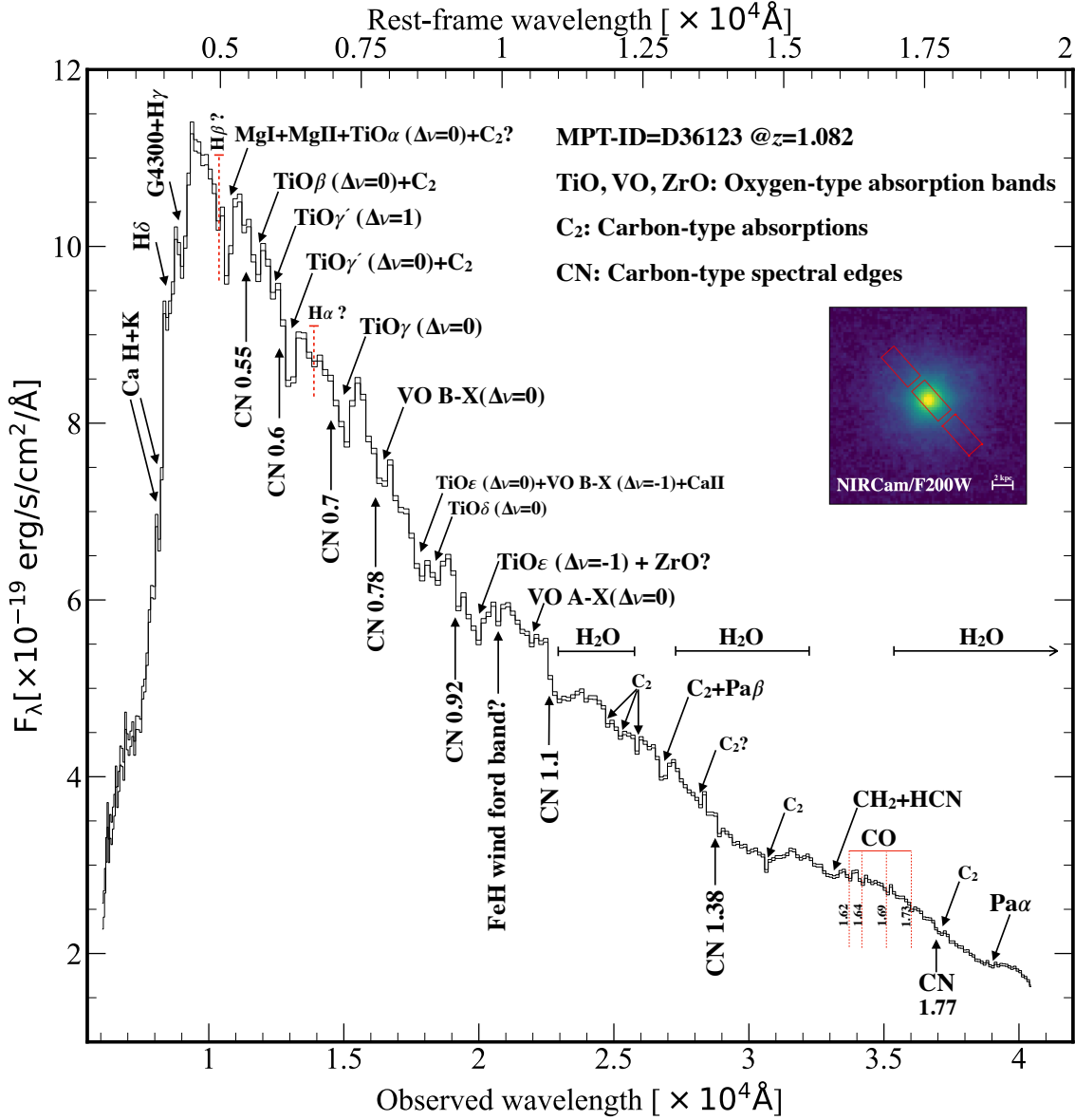


Figure 1: **NIR rest-frame spectrum of the quiescent galaxy D36123 at $z=1.082$.** The upper and lower histograms display the 1σ uncertainty range (notice the high SNR). The rest-frame wavelengths are calculated from the redshift corresponding to the best fit of M13 models. Black arrows point to identifications of oxygen-type and carbon-type absorption and to the detections of deep CN edges. Both sets of features are characteristic of carbon-rich and oxygen-rich stars in the TP-AGB phase. The question mark indicates uncertain features. The NIRCams image in the F200W band is shown in the inset together with the NIRSPEC shutters layout (each shutter is $0.2'' \times 0.46''$).

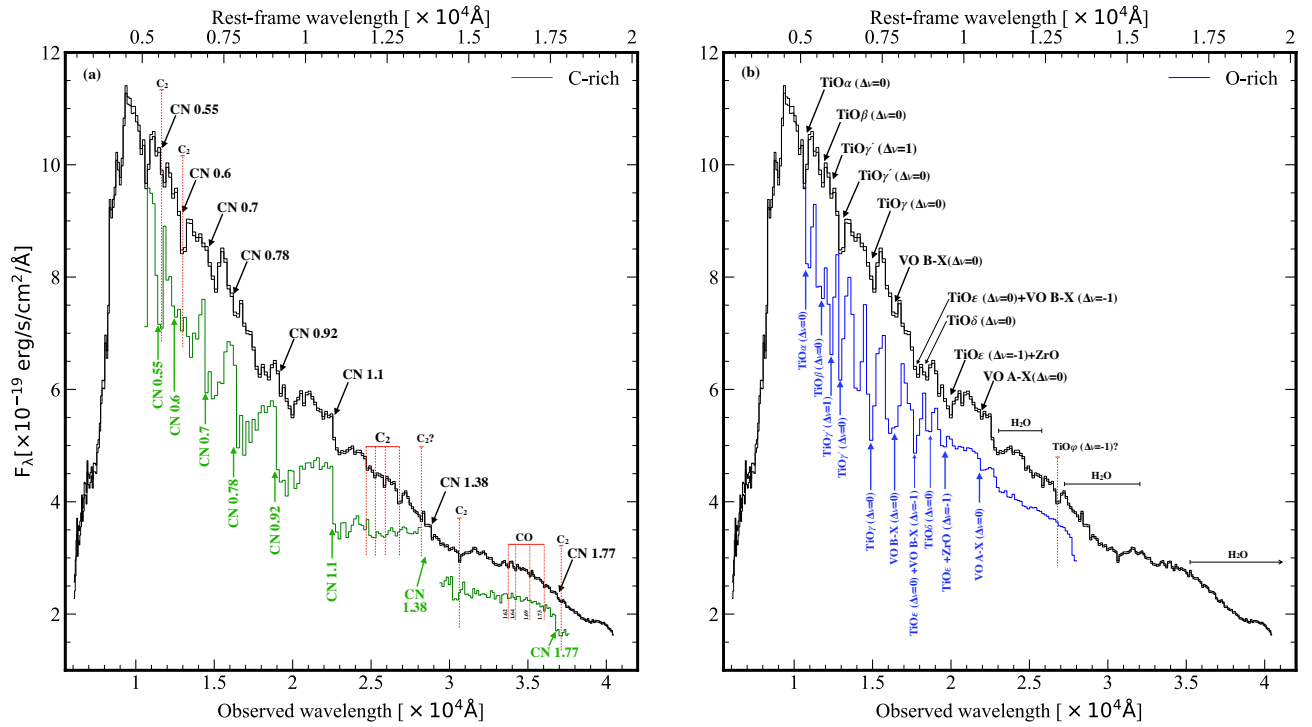


Figure 2: **TP-AGB features identification on D36123 based on Milky-Way stars.** (a) The deep CN edges and carbon-containing molecules are confirmed by comparing them to a C-rich (C1) star¹⁴ (in green) in the TP-AGB phase. (b) The TiO, VO, and ZrO absorptions are identified as stemming from a O-rich star (in the coldest bin¹³, shown in blue) in the TP-AGB phase. For easing the comparison the stellar spectra are stretched to follow the continuum shape of our high redshift target.

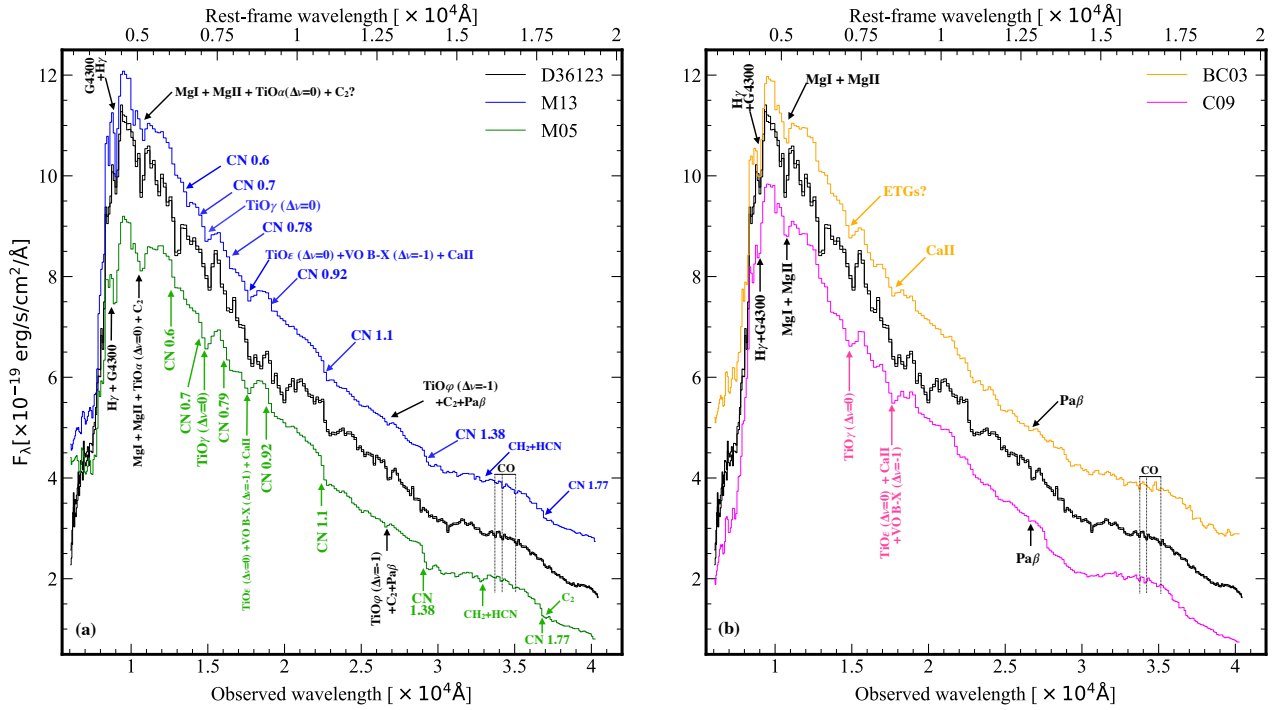


Figure 3: **Fitting the D36123 spectrum with stellar population models.** (a) The TP-AGB-mild (M13, blue) and TP-AGB-heavy (M05, green) models. (b) The TP-AGB-poor (BC03, orange) and TP-AGB-light (C09, magenta) models. All best fitting models are additively shifted for clarity. The black histograms show the observed spectrum of D36123 and its errors. Black arrows/labels highlight features identified by all four models at the same absorption positions. Two absorption features in orange (in magenta) are identified by BC03 (C09) model. Other CN edges and oxygen-type absorptions can be identified by M13 and M05 models.

Table 1: Stellar population properties of D36123.

Rest-frame spectral range	Property	BC03	C09	M13	M05
		TP-AGB-poor	TP-AGB-light	TP-AGB-mild	TP-AGB-heavy
		RA = 14h : 19m : 34.258s		DEC = +52° : 56' : 23.079''	
full (0.3–2 μ m)	redshift	1.074 ^{+0.001} _{-0.001}	1.075 ^{+0.003} _{-0.001}	1.082 ^{+0.002} _{-0.002}	1.075 ^{+0.002} _{-0.004}
	$M_* [\times 10^{10} M_\odot]$	1.493 ^{+0.007} _{-0.004}	1.489 ^{+0.007} _{-0.006}	1.167 ^{+0.008} _{-0.005}	1.552 ^{+0.015} _{-0.014}
	age [Gyr]	1.661 ^{+0.024} _{-0.041}	0.751 ^{+0.025} _{-0.034}	0.621 ^{+0.029} _{-0.021}	2.224 ^{+0.016} _{-0.024}
	Z/Z_\odot	1.944 ^{+0.028} _{-0.034}	2.000 ^{+0.000} _{-0.008}	1.589 ^{+0.061} _{-0.039}	0.982 ^{+0.001} _{-0.001}
	A_v	0.000 ^{+0.002} _{-0.000}	0.156 ^{+0.016} _{-0.022}	0.424 ^{+0.026} _{-0.026}	0.000 ^{+0.000} _{-0.000}
	τ [Gyr]	0.241 ^{+0.019} _{-0.018}	0.104 ^{+0.014} _{-0.021}	0.100 ^{+0.010} _{-0.010}	0.707 ^{+0.013} _{-0.017}
	$SFR_{best} [M_\odot/\text{yr}]$	0.294 ^{+0.036} _{-0.065}	0.099 ^{+0.001} _{-0.001}	0.311 ^{+0.003} _{-0.003}	1.320 ^{+0.006} _{-0.006}
	SFR_{best}/SFR_{peak}	0.019 ^{+0.011} _{-0.010}	0.014 ^{+0.022} _{-0.015}	0.024 ^{+0.024} _{-0.023}	0.368 ^{+0.032} _{-0.024}
	χ_R^2	59.6	52.9	39.0	102.6
optical ($< 0.5\mu$ m)	redshift	1.078 ^{+0.002} _{-0.002}	1.083 ^{+0.001} _{-0.002}	1.078 ^{+0.001} _{-0.002}	1.078 ^{+0.001} _{-0.002}
	$M_* [\times 10^{10} M_\odot]$	1.330 ^{+0.019} _{-0.013}	1.406 ^{+0.033} _{-0.043}	1.140 ^{+0.011} _{-0.197}	1.151 ^{+0.024} _{-0.021}
	age [Gyr]	0.961 ^{+0.021} _{-0.026}	0.810 ^{+0.005} _{-0.003}	0.909 ^{+0.098} _{-0.098}	0.969 ^{+0.031} _{-0.069}
	Z/Z_\odot	1.525 ^{+0.095} _{-0.225}	2.000 ^{+0.000} _{-0.007}	2.183 ^{+0.017} _{-0.041}	1.002 ^{+0.048} _{-0.052}
	A_v	0.068 ^{+0.082} _{-0.068}	0.000 ^{+0.034} _{-0.000}	0.000 ^{+0.038} _{-0.000}	0.000 ^{+0.002} _{-0.000}
	τ [Gyr]	0.007 ^{+0.017} _{-0.006}	0.091 ^{+0.025} _{-0.026}	0.001 ^{+0.010} _{-0.000}	0.007 ^{+0.043} _{-0.000}
	$SFR_{best} [M_\odot/\text{yr}]$	0.000 ^{+0.004} _{-0.000}	0.093 ^{+0.001} _{-0.001}	0.000 ^{+0.006} _{-0.000}	0.000 ^{+0.010} _{-0.000}
	SFR_{best}/SFR_{peak}	~ 0	~ 0	~ 0	~ 0
	χ_R^2	11.4	9.0	11.2	11.2
NIR ($> 0.5\mu$ m)	redshift	1.074 ^{+0.001} _{-0.001}	1.080 ^{+0.002} _{-0.004}	1.083 ^{+0.002} _{-0.002}	1.080 ^{+0.003} _{-0.001}
	$M_* [\times 10^{10} M_\odot]$	1.679 ^{+0.023} _{-0.031}	1.514 ^{+0.028} _{-0.021}	1.247 ^{+0.038} _{-0.017}	0.556 ^{+0.010} _{-0.004}
	age [Gyr]	1.961 ^{+0.011} _{-0.039}	0.783 ^{+0.031} _{-0.028}	0.490 ^{+0.041} _{-0.041}	0.207 ^{+0.014} _{-0.001}
	Z/Z_\odot	1.883 ^{+0.040} _{-0.034}	2.000 ^{+0.000} _{-0.016}	0.692 ^{+0.029} _{-0.032}	0.500 ^{+0.022} _{-0.000}
	A_v	0.000 ^{+0.006} _{-0.000}	0.103 ^{+0.022} _{-0.022}	0.706 ^{+0.049} _{-0.044}	0.982 ^{+0.029} _{-0.012}
	τ [Gyr]	0.497 ^{+0.029} _{-0.032}	0.057 ^{+0.016} _{-0.017}	0.023 ^{+0.010} _{-0.010}	2.605 ^{+0.332} _{-0.316}
	$SFR_{best} [M_\odot/\text{yr}]$	0.984 ^{+0.177} _{-0.148}	0.000 ^{+0.012} _{-0.000}	0.000 ^{+0.018} _{-0.000}	23.725 ^{+0.013} _{-0.104}
	SFR_{best}/SFR_{peak}	0.207 ^{+0.057} _{-0.049}	~ 0	~ 0	0.200 ^{+0.029} _{-0.024}
	χ_R^2	60.7	58.5	40.7	66.6
full (excluding 0.5–1 μ m)	redshift	1.076 ^{+0.001} _{-0.001}	1.093 ^{+0.001} _{-0.002}	1.081 ^{+0.001} _{-0.001}	1.075 ^{+0.002} _{-0.003}
	$M_* [\times 10^{10} M_\odot]$	1.581 ^{+0.015} _{-0.014}	1.750 ^{+0.087} _{-0.002}	1.076 ^{+0.008} _{-0.002}	1.535 ^{+0.021} _{-0.025}
	age [Gyr]	1.627 ^{+0.021} _{-0.019}	1.446 ^{+0.095} _{-0.046}	0.712 ^{+0.018} _{-0.012}	2.183 ^{+0.038} _{-0.040}
	Z/Z_\odot	2.300 ^{+0.048} _{-0.036}	0.300 ^{+0.010} _{-0.009}	1.285 ^{+0.030} _{-0.023}	0.990 ^{+0.007} _{-0.007}
	A_v	0.000 ^{+0.004} _{-0.000}	0.078 ^{+0.023} _{-0.017}	0.068 ^{+0.014} _{-0.013}	0.000 ^{+0.009} _{-0.000}
	τ [Gyr]	0.028 ^{+0.012} _{-0.008}	0.127 ^{+0.054} _{-0.065}	0.095 ^{+0.009} _{-0.010}	0.690 ^{+0.012} _{-0.014}
	$SFR_{best} [M_\odot/\text{yr}]$	0.000 ^{+0.008} _{-0.000}	0.000 ^{+0.045} _{-0.000}	0.084 ^{+0.013} _{-0.012}	1.306 ^{+0.022} _{-0.010}
	SFR_{best}/SFR_{peak}	~ 0	~ 0	0.011 ^{+0.009} _{-0.008}	0.363 ^{+0.027} _{-0.022}
	χ_R^2	32.2	23.1	16.3	83.7

The 1st column denotes the rest-frame range of wavelength adopted in the spectral fit. The 3rd to 6th columns list the best-fitting physical properties derived by four models with different TP-AGB treatments. Specifically, the total stellar masses are based on the Chabrier⁵⁵ IMF. The best-fitting parameters and errors are derived from the distribution of χ^2 , with the former obtained at χ^2 -minimisation, and the errors determined after rescaling to $\chi_R^2 = 1$. SFR_{best}/SFR_{peak} is a measure of quiescence, where the SFR_{best} is derived from the best fit by adopting delay- τ models, and the SFR_{peak} is corresponding to the SFR maximum at $t = \tau$.

Table 2: Stellar population properties of galaxies 8595 and 9025.

Target (Rest-frame)	Property	BC03 TP-AGB-poor	C09 TP-AGB-light	M13 TP-AGB-mild	M05 TP-AGB-heavy
		RA = 14h : 20m : 42.240s		DEC = +53° : 01' : 50.298''	
8595 (full)	redshift	$1.739^{+0.004}_{-0.002}$	$1.746^{+0.002}_{-0.003}$	$1.746^{+0.002}_{-0.003}$	$1.741^{+0.002}_{-0.002}$
	$M_* [\times 10^{10} M_\odot]$	$0.791^{+0.020}_{-0.020}$	$0.736^{+0.009}_{-0.007}$	$0.545^{+0.003}_{-0.003}$	$0.676^{+0.009}_{-0.009}$
	age [Gyr]	$1.913^{+0.052}_{-0.052}$	$0.798^{+0.023}_{-0.023}$	$0.732^{+0.028}_{-0.027}$	$1.908^{+0.057}_{-0.058}$
	Z/Z_\odot	$1.711^{+0.039}_{-0.039}$	$2.000^{+0.000}_{-0.006}$	$1.584^{+0.044}_{-0.046}$	$1.878^{+0.012}_{-0.012}$
	Av	$0.012^{+0.051}_{-0.012}$	$0.357^{+0.023}_{-0.030}$	$0.368^{+0.020}_{-0.021}$	$0.013^{+0.022}_{-0.013}$
	τ [Gyr]	$0.283^{+0.029}_{-0.034}$	$0.134^{+0.041}_{-0.048}$	$0.133^{+0.038}_{-0.055}$	$0.403^{+0.022}_{-0.025}$
	$SFR_{best} [M_\odot/\text{yr}]$	$0.073^{+0.015}_{-0.015}$	$0.049^{+0.004}_{-0.004}$	$0.061^{+0.004}_{-0.004}$	$0.232^{+0.019}_{-0.018}$
	SFR_{best}/SFR_{peak}	$0.021^{+0.018}_{-0.015}$	$0.042^{+0.078}_{-0.078}$	$0.061^{+0.142}_{-0.098}$	$0.113^{+0.038}_{-0.034}$
	χ^2_R	0.821	0.950	0.794	0.935
	$P(\Delta\chi^2)$	0.00103	0	–	0
		RA = 14h : 19m : 33.991s		DEC = +52° : 51' : 56.290''	
9025 (full+HST)	redshift	$1.545^{+0.001}_{-0.001}$	$1.546^{+0.001}_{-0.002}$	$1.569^{+0.001}_{-0.002}$	$1.569^{+0.001}_{-0.002}$
	$M_* [\times 10^{10} M_\odot]$	$0.759^{+0.082}_{-0.046}$	$0.859^{+0.087}_{-0.042}$	$0.755^{+0.052}_{-0.050}$	$0.746^{+0.025}_{-0.023}$
	age [Gyr]	$1.560^{+0.073}_{-0.122}$	$1.580^{+0.065}_{-0.062}$	$0.272^{+0.045}_{-0.045}$	$0.182^{+0.001}_{-0.018}$
	Z/Z_\odot	$2.123^{+0.203}_{-0.075}$	$0.300^{+0.004}_{-0.003}$	$1.700^{+0.115}_{-0.124}$	$1.140^{+0.064}_{-0.045}$
	Av	$0.351^{+0.061}_{-0.103}$	$0.397^{+0.026}_{-0.025}$	$1.125^{+0.048}_{-0.042}$	$1.337^{+0.052}_{-0.046}$
	τ [Gyr]	$0.304^{+0.037}_{-0.042}$	$0.316^{+0.063}_{-0.071}$	$0.019^{+0.008}_{-0.010}$	$0.008^{+0.006}_{-0.007}$
	$SFR_{best} [M_\odot/\text{yr}]$	$0.181^{+0.024}_{-0.013}$	$0.230^{+0.045}_{-0.028}$	$0.048^{+0.014}_{-0.014}$	$0.027^{+0.004}_{-0.004}$
	SFR_{best}/SFR_{peak}	$0.082^{+0.068}_{-0.056}$	$0.092^{+0.107}_{-0.095}$	~0	~0
	χ^2_R	1.702	1.838	1.634	1.649
	$P(\Delta\chi^2)$	0.00001	0	–	0.03767

For both objects, the spectral fit utilizes the entire rest-frame wavelength range. Additionally, to better constrain the age-sensitive wavelength around 4000Å, two additional HST bands (F606W+F814W) are employed simultaneously in the fit of object 9025 (see Methods). Measurements and errors are as in Tab.1, except that we did not rescale the reduced χ^2 to 1. $\Delta\chi^2$ is computed relative to the M13 model.

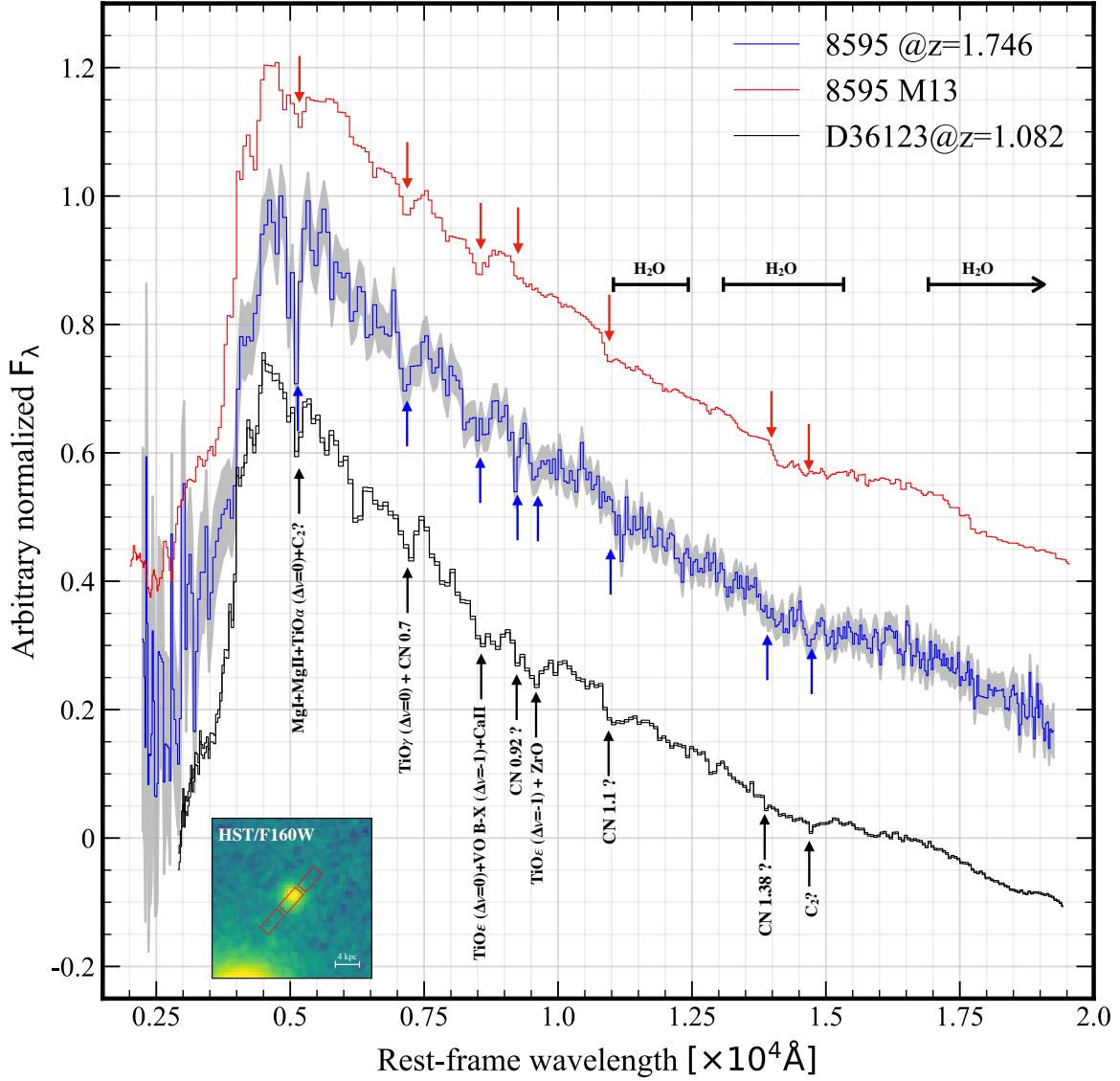


Figure 4: **NIR spectrum and features identification for galaxy 8595.** The observed spectrum of galaxy 8595 (blue) with error (grey shaded region) is compared with the M13 best-fitting model (red), alongside the spectrum of the bright galaxy D36123 (black), to identify features (The comparison spectra are shifted up or down additively for clarity.). Matched features (labelled) in the NIR spectra of object 8595 are indicated by blue arrows. Most features predicted by the M13 model are indicated by red arrows. Tentative identifications are shown by a question mark. The HST/F160W image is displayed in the lower-left corner, with NIRSpect shutters overlaid.

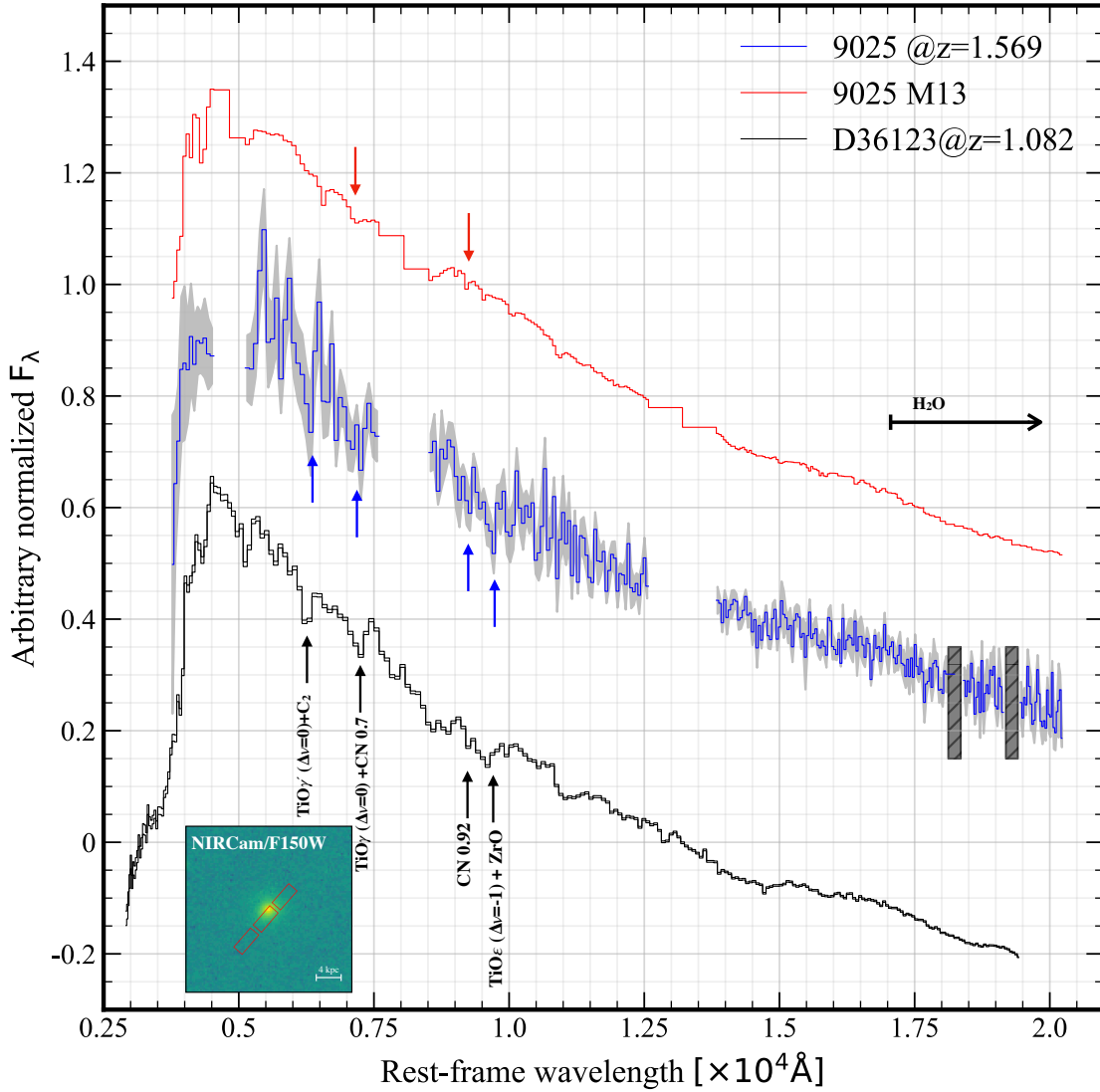


Figure 5: **NIR spectrum and features identification for galaxy 9025.** Analogous to the previous figure. Note that the observed median resolution spectrum of 9025 has been resampled to the PRISM spectral pixel grid in this figure to increase SNR and clarity. Some contaminated regions are blanked in the redder part of the spectrum. The lower left corner shows the NIRCcam/F150W image together with NIRSPEC shutters layout, from which the sub-optimal centering of this galaxy can be noticed.

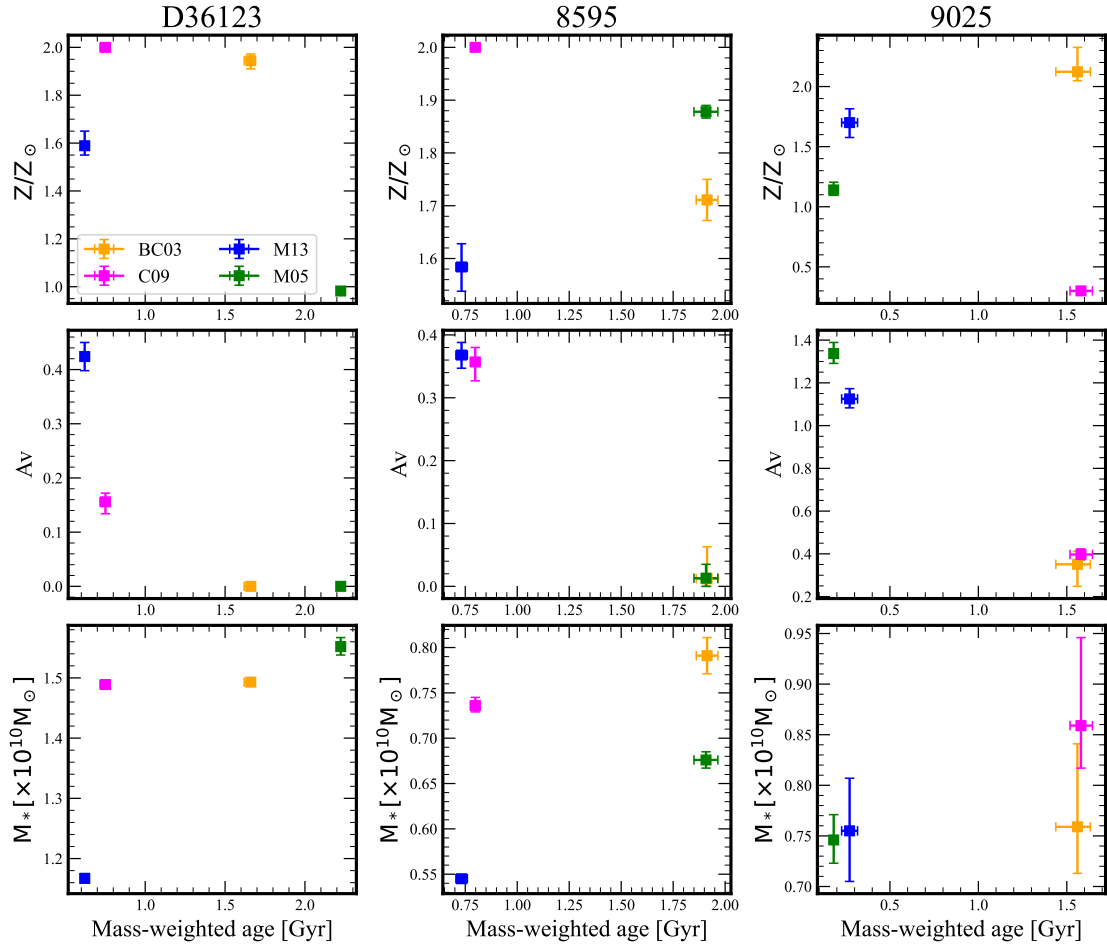


Figure 6: **Comparison of best fitting results from the different models.** Ages are shown as a function of metallicity (Z/Z_{\odot} , top), reddening (A_V , middle), and stellar mass (M_* , bottom) for the full-range spectral fitting. The panels from left to right correspond to objects D36123, 8595, and 9025. The results based on different models are shown in different colors. The error bars for object D36123 are obtained after rescaling the reduced χ^2 to 1.

4 Methods

NIRSpec observation and reduction

In this study, we present NIR spectra for three quiescent galaxies, IDs=D36123, 8595, and 9025. We cross-matched the catalog in CANDELS EGS field ²² with the NIRSpec detections in the DD-ERS-1345 (CEERS, PI: Steven Finkelstein) and DD-2075 (PI: Pablo Arrabal Haro) programs. Both D36123 and 8595 were observed with the PRISM ⁵⁶, spanning 0.60-5.30 μ m with varying spectral resolution $R \equiv \lambda/\Delta\lambda \approx 30$ at $\lambda = 1.2\mu$ m to $R > 300$ at $\lambda > 5\mu$ m. Object 9025 was observed with the G140M/F100LP, G235M/F170LP, and G395M/F290LP medium-resolution ($R=500-1340$) gratings⁵⁶, covering 0.7-5.2 μ m. Three-shutter slitlets were employed, enabling a three-point nodding pattern to facilitate background subtraction. The total exposure time on sources 8595 and 9025 are the same at 3107s, while on source D36123 it is 18387s ($\sim 6\times$ higher).

The NIRSpec data processing followed the same methodology as used for other CEERS NIRSpec observations ^{27,28,57-59}. The NIRSpec data reduction was based on the STScI Calibration Pipeline ⁶⁰ version 1.8.5 and the Calibration Reference Data System (CRDS) mapping 1041 for objects 8595 and 9025, and CRDS mapping 1029 for D36123. There are three main stages in the reduction process. Briefly, the `calwebb_detector1` pipeline module was utilized to correct for the detector 1/f noise, subtract the bias and dark current, generate the count-rate maps (CRMs) from the uncalibrated images. There is an improvement in the `jump` step to correct the cosmic ray “snowball” ²⁸. The stage two of the pipeline reduction is to create two-dimensional (2D) spectra with a rectified trace and flat slope from the generated CRMs. The background subtraction and slit loss correction of objects D36123 and 8595 were considered at this stage, while the slit loss correction (`pathloss`) was not taken into account for object 9025 as it is poorly centered in the shutter. We verified that better overall χ^2_R of its spectral fit can be obtained if adopting the empirical aperture corrections directly, which is the last step of the absolute flux calibrations (as discussed later in a dedicated subsection) to complement any incorrect calibration during the reduction process. At the third stage, we made use of optimised apertures for the extraction of the one-dimensional (1D) spectra in all cases. For object D36123, we adopted a 4-pixel extraction aperture, considering the effects of the Micro-Shutter Assembly ⁶¹ (MSA) bar shadows on some upper pixels in 2D spectra. We also considered 3- and 5-pixel apertures, with negligible impact on the results. The flux error for the extracted spectra was calculated by the JWST pipeline using an instrumental noise. We rescaled all flux errors multiplying by a factor of ~ 1.5 to account for correlations induced by the pipeline ²⁷.

Table 3: Structural parameters.

	D36123	8595	9025
	F150W	F160W	F150W
r_e''	0.085 ± 0.001	0.087 ± 0.010	0.125 ± 0.001
n	3.713 ± 0.025	3.020 ± 0.823	2.088 ± 0.031
b/a	0.975 ± 0.003	0.900 ± 0.090	0.771 ± 0.031
PA $^\circ$	1 ± 3	43 ± 38	-57 ± 1
Mag _{AB}	21.97 ± 0.01	24.22 ± 0.09	23.70 ± 0.01

The spectrum of 9025, observed with 3 medium-resolution gratings, was calibrated through several steps. We first matched the 3 spectra scaling them by a constant term, determined using the overlapping regions, with variance weighting. This required a scaling of factors of 1.23 and 1.28 between G140M and G235M and between G235M and G395M, respectively. In the overlapping regions, the final coadded spectra were obtained by combining their weighted spectra and errors, ensuring that standard errors in the weighted mean over common wavelength ranges remained unchanged after resampling. For the purpose of increasing the continuum SNR to display the NIR features and speeding up the spectral fit computation, we finally resampled this medium-resolution spectrum to the one in the PRISM resolution. The average flux and the standard error of the mean in each PRISM wavelength bin were adopted.

Photometric measurements

Two out of three galaxies (D36123 and 9025) were observed in CEERS/NIRCam ⁶² imaging, while all (including 8595) have CANDELS/HST ^{23,24} imaging. We used `galfit` ^{63,64} to derive their structure and obtain photometry in NIRCam bands (such as F115W, F150W, F200W, F277W, F356W, F410W, and F444W, when available), in HST bands (such as F606W, F814W, F125W, F140W, F160W, when needed) and in CFHT/WIRCam Ks band (only for object 8595). We adopted $3'' \times 3''$ -wide cutouts with $0.03''\text{pix}^{-1}$ sampling in the NIRCam bands and $0.06''\text{pix}^{-1}$ sampling in the HST bands. We fitted the galaxies by using single Sérsic models with free parameters, including the positions, Sérsic index (n), effective radius (r_e), total magnitudes, axis ratio (b/a), and position angle (PA). The point spread functions (PSFs) in different NIRCam bands were adopted from previous CEERS work ⁶⁵. They were constructed by stacking point sources using the software `PSFEX` ⁶⁶. We carefully modeled all objects in the field of view, with special attention in the case of 8595 in the $5'' \times 5''$ region to a bright nearby galaxy. We took about 5% systematic uncertainty of photometry into account for objects D36123 and 9025, while 10% systematic uncertainty of photometry was adopted for object 8595 when considering the effect of the bright nearby galaxy. The structural parameters (D36123 and 9025 in F150W and 8595 in F160W) are listed in Table 3. Fig.7 shows the `galfit` models and residuals.

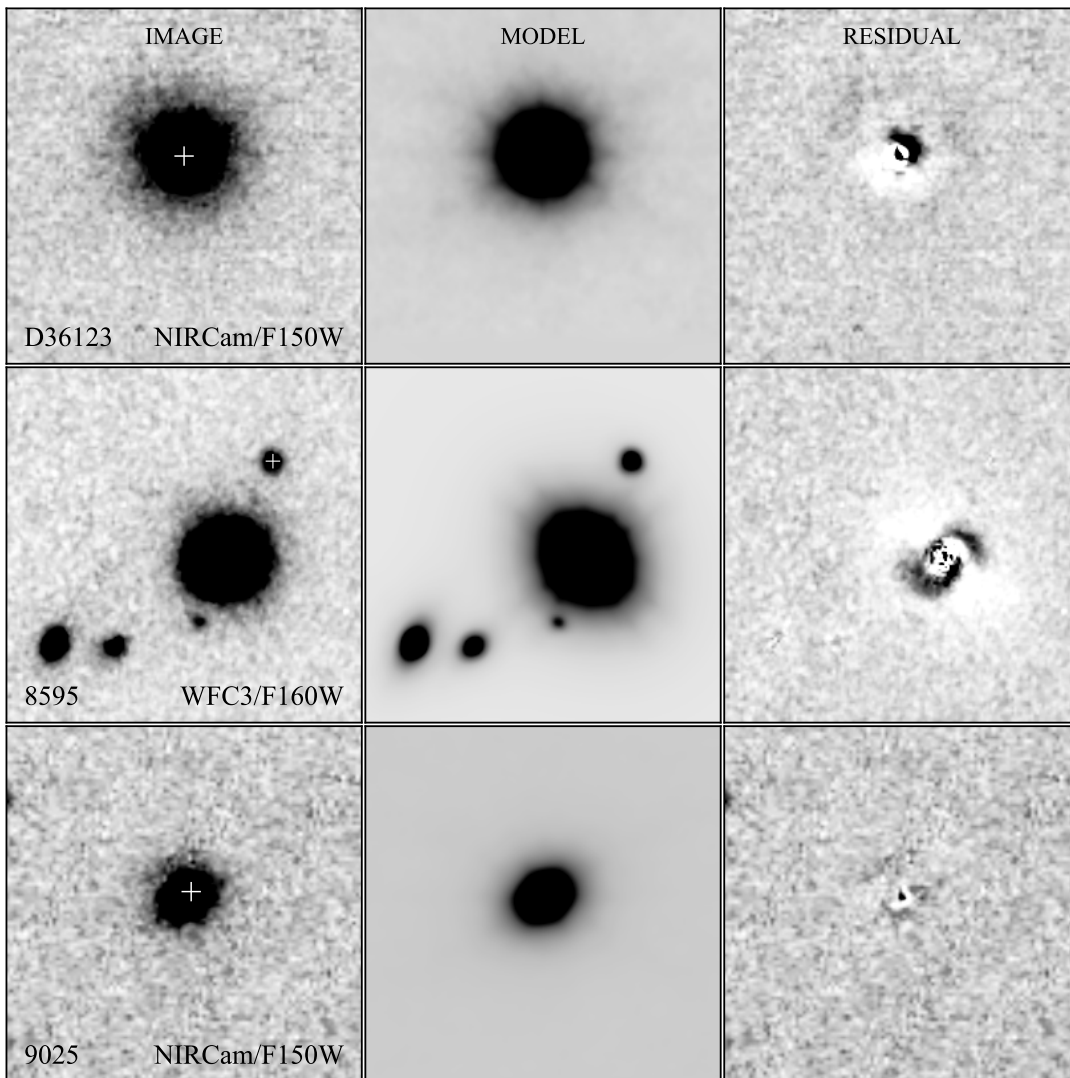


Figure 7: **Example of `galfit` results.** The original image, best-fit model, and residual of object D36123 in NIRCcam/F150W are shown in the top row. The results of objects 8595 in WFC3/F160W and 9025 in NIRCcam/F150W are presented in the middle and bottom rows, respectively. The three targets are marked by white crosses on the original images (notice that 8595 is not at the center of the cutout). The cutouts of objects D36123 and 9025 are $3'' \times 3''$ wide, with a scale of $0.03''\text{pix}^{-1}$. The cutouts for object 8595 are $5'' \times 5''$ wide with a pixel scale of $0.06''\text{pix}^{-1}$.

Aperture correction

Spectra reduced with the NIRSpec pipeline include an aperture correction term that is derived assuming a point-source scenario. To account for the actual shapes of our galaxies, we integrate the observed spectra through imaging filter bandpasses to obtain synthetic photometry (i.e., F_{syn}), and compare to the actual photometry (i.e., F_{phot}) measured from imaging. We are implicitly assuming here that no strong color gradient biases the in-slit photometry with respect to the integrated galaxy photometry. This point has been verified by building PSF-matched color images of our targets and verifying that no color-gradients were apparent. We thus derive the aperture correction as $R_{corr} = F_{phot}/F_{syn}$. The top panel of Fig.8 shows the aperture correction for object D36123 derived in this way. We adopt a linear function to fit the trend with wavelength, as shown by the red line. There is a weak wavelength dependence (slope $\alpha \sim 0.02$). The green line presents the rescaled aperture correction derived from the forward-modeling tool for NIRSpec Multi-Object Spectroscopic data, namely MSAFIT⁶⁷, which accounts for the complex geometry of the target galaxy, point spread function and pixelation of the NIRSpec instrument. This MSAFIT line aligns with the red linear relation. Regardless of the relation (linear vs. MSAFIT) or when adopting the extremes in the $\pm 1\sigma$ range in the linear relation (the grey shaded region of D36123 in Fig.8) to correct the spectrum, the best-fit parameters and spectral fits show minimal changes. Hence we decided to finally rescale the observed spectrum of D36123 by adopting the linear relation. The same process is applied to the other two objects 8595 and 9025. Their spectra are rescaled multiplying by a constant value of ~ 2.28 and a linear relation with a slope of ~ -0.07 , respectively.

Spectral resolution

When comparing the observed spectra with spectral synthesis models we need to match their spectral resolution. For the observed spectra, we have to consider the instrumental broadening, as well as the intrinsic linewidths from the galaxies. For the template models, we need to estimate their intrinsic spectral resolution. We will discuss in turn these terms in the following.

The spectral resolution of the NIRSpec PRISM is relatively low. Based on the spectral sampling and for an unresolved source filling the slit, we can expect a resolution of 70 at $0.6\mu\text{m}$, declining to 30 at $1.1\mu\text{m}$, and rising again to 200 at $5\mu\text{m}$. For point/compact sources, the resolution of in-flight data could be $1.5\text{-}2.0\times$ higher than that in the pre-launch approximation⁶⁷. This would be helpful to identify some weak/narrower features, especially for galaxy D36123 where the SNR in the continuum is high. We adopt the MSAFIT⁶⁷ software to model the NIRSpec resolving power based on the actual galaxy spatial profile. The resolution modeled by MSAFIT software is consistent with that of a

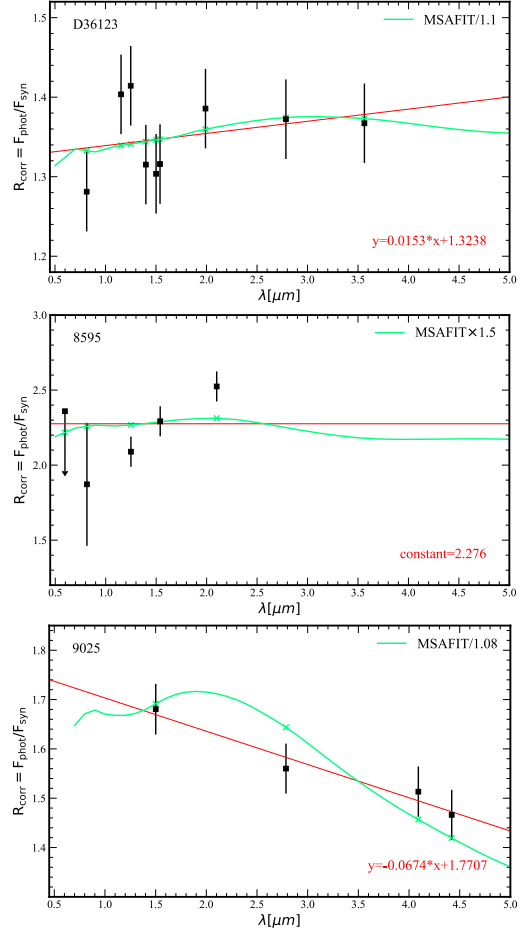


Figure 8: **Aperture correction.** Aperture correction (R_{corr}) in different bands as obtained through the ratio of the measured imaging photometry (F_{phot}) to the synthetic photometry (F_{syn}). The latter is obtained by integrating the spectra through the filter bandpasses. Panels from top to bottom show aperture corrections for objects D36123, 8595, and 9025. The aperture corrections adopted for the reported analysis are shown in red (after checking that no meaningful change follow from adopting the alternative shapes). The gray shaded region for object D36123 (which has a much higher SNR) presents the uncertainty on the linear aperture correction relation. The adoption of relations within the $\pm 1\sigma$ range also lead to no significant change in the result. The green curves are derived by the MSAFIT⁶⁷ code, based on the measured size and Sérsic profiles for our targets.

flat source in a slit width of 1.4 pixels (see green curve in the top-middle panel of Fig.9).

The intrinsic dispersion of our target early-type galaxies (ETGs) need to be accounted next. The velocity dispersion σ can be estimated using local stellar mass vs. velocity dispersion relations (i.e., M_* - σ) relation³⁵. We convert σ to the full width at half maximum (FWHM) and define $1/R = v_{(\text{rest,FWHM})}/c = \Delta\lambda/\lambda$ (where $\Delta\lambda = \text{FWHM}$). The intrinsic broadening of an ETG with a velocity dispersion $\sim 130\text{km/s}$ (a ballpark number for the typical masses $\sim 10^{10} M_\odot$ in our study) corresponds to $R \sim 1000$ (see the grey line in the top-middle panel of Fig.9), quite negligible compared to the instrumental spread.

Finally, we estimated the template model's resolution from their spectral sampling, adopting 2 spectral bin widths as their (Nyquist) sampling. The sampling (hence resolution) is changing in steps, higher in the optical than in the NIR. Redshifting will affect where these steps actually apply for the observed galaxies. The corresponding resolution in the observed frame for D36123 (assuming an average $z \sim 1.077$), is shown in the top-middle panel of Fig.9.

To match the resolution of the models with the observed spectrum, we need to account for all three impacting factors: prism dispersion (dominant term), the wavelength sampling of the spectral template models, and the velocity dispersion of the ETG. We add and subtract in quadrature the corresponding terms at fixed λ_{obs} . The broadening $\Delta\lambda_{\text{fit}}$ needed to be applied to models to match the observed spectra is provided by the formula:

$$\Delta\lambda_{\text{fit}} = \sqrt{\Delta\lambda_{\text{PRISM}(1.4 \text{ pix})}^2 - \Delta\lambda_{\text{MOD}_i}^2 + \Delta\lambda_{\text{ETG}}^2}, \quad (1)$$

where i refers to the model. The final smoothing functions applied to models are equivalent to resolutions among ranging from $R \sim 60$ to 450 across observed wavelength range of 0.6–3.3 μm , as depicted in the top right panel of Fig.9. Beyond $\sim 3.3\mu\text{m}$ we are limited by the models resolution and therefore no further smoothing is applied to them. We repeat similar procedures to obtain the appropriate smoothing kernels for objects 8595 and 9025, shown in the middle and bottom panels of Fig.9. For both, the prism resolution is based on 1.4-pixel elements, and the spectra in different models was resampled in every 2 spectral bin widths, similar to what is done for object D36123.

Spectral fit

To estimate the stellar mass, age, and SFH of a galaxy, we adopt a custom IDL routine⁶⁸ to fit the final corrected 1D spectrum of each galaxy. The best-fitting results are derived by comparing the 1D spectrum with a range of composite stellar population templates by χ^2 -minimisation. These templates were generated by combining a grid of different SSP models assuming a delayed exponentially declining SFH

($\propto (t/\tau^2)e^{-t/\tau}$, i.e., delayed- τ model). The characteristic timescale τ and age variations are the same in different models, shown in Table 4. To identify the redshift, the Calzetti attenuation law⁶⁹ was adopted, and the stellar metallicity was left free with lower and upper limits dependent on the model. To reduce the computational cost, we run the spectral fit twice. First, we run the spectral fit in a large range of redshift with a low-resolution grid ($\Delta z = 0.1$). After the most probable redshift peak was identified, we narrowed down the redshift range with a high-resolution grid ($\Delta z = 0.001$) in the second run. The redshift boundary in Table 4 is an example of a parametric grid for D36123 in the second run. For object D36123 with the highest SNR, the spectral fit was repeated varying the wavelength range (see Table 1): (1) with the full rest-frame wavelength (0.3–2 μm , see Fig 10); (2) with the optical only ($\lambda_{\text{rest}} < 0.5\mu\text{m}$); (3) with the NIR only ($\lambda_{\text{rest}} > 0.5\mu\text{m}$); and (4) with the full rest-frame wavelength range but excluding 0.5–1 μm (see Fig. 11). For the two fainter galaxies, the spectral fit was only done in the full rest-frame wavelength. Since the medium resolution grating spectrum of object 9025 does not cover too well the age-sensitive spectral region around rest-frame 4000 \AA break, we additionally considered the photometry in HST F606W and F814W bands to better constrain the overall fit.

The best-fitting parameters with 1σ errors⁷⁰ can be derived from the distribution of χ^2 , which are listed in Table 2. Considering the large minimum reduced χ^2 of object D36123, we derived the uncertainties (as listed in Table 1) scaling up all errors to obtain a $\chi^2_R \sim 1.0$. All stellar masses are reported for a Chabrier IMF⁵⁵, and are corrected for stellar losses and include remnants. Fig.10 shows the best-fit model for each galaxy using different models in red at the top of each panel, and the relative flux deviation $D_{\text{REL}} = (F_{\lambda,\text{obs}} - F_{\lambda,\text{mod}})/F_{\lambda,\text{obs}}$ at the bottom of each panel. The SNR-weighted averages of the relative deviations are labeled in the top-right corner of each bottom-panel. For object D36123 the models deviate from the spectrum at a few percent level (2.5% level for M13, and higher values for the other models). This is likely driven by systematics in the models (plus, possible residual calibration errors) which we can detect at the high SN ratio. Higher deviations correspond to observed features not matched by the models. For the other galaxies the relative flux deviations are larger and dominated by the noise in the data.

Additional details on models

The C09 models allow several user options and have been modified through the years. The models used in this work were generated using the latest FSPS version 3.2 by adopting a Chabrier IMF, the BaSTI isochrones and the MILES stellar library, without considering dust extinction. We correct for the expected stellar losses and include remnants. The C09 models include TP-AGB spectra, extrapolated blueward with simpler linear slopes (as advocated by Lancon & Wood

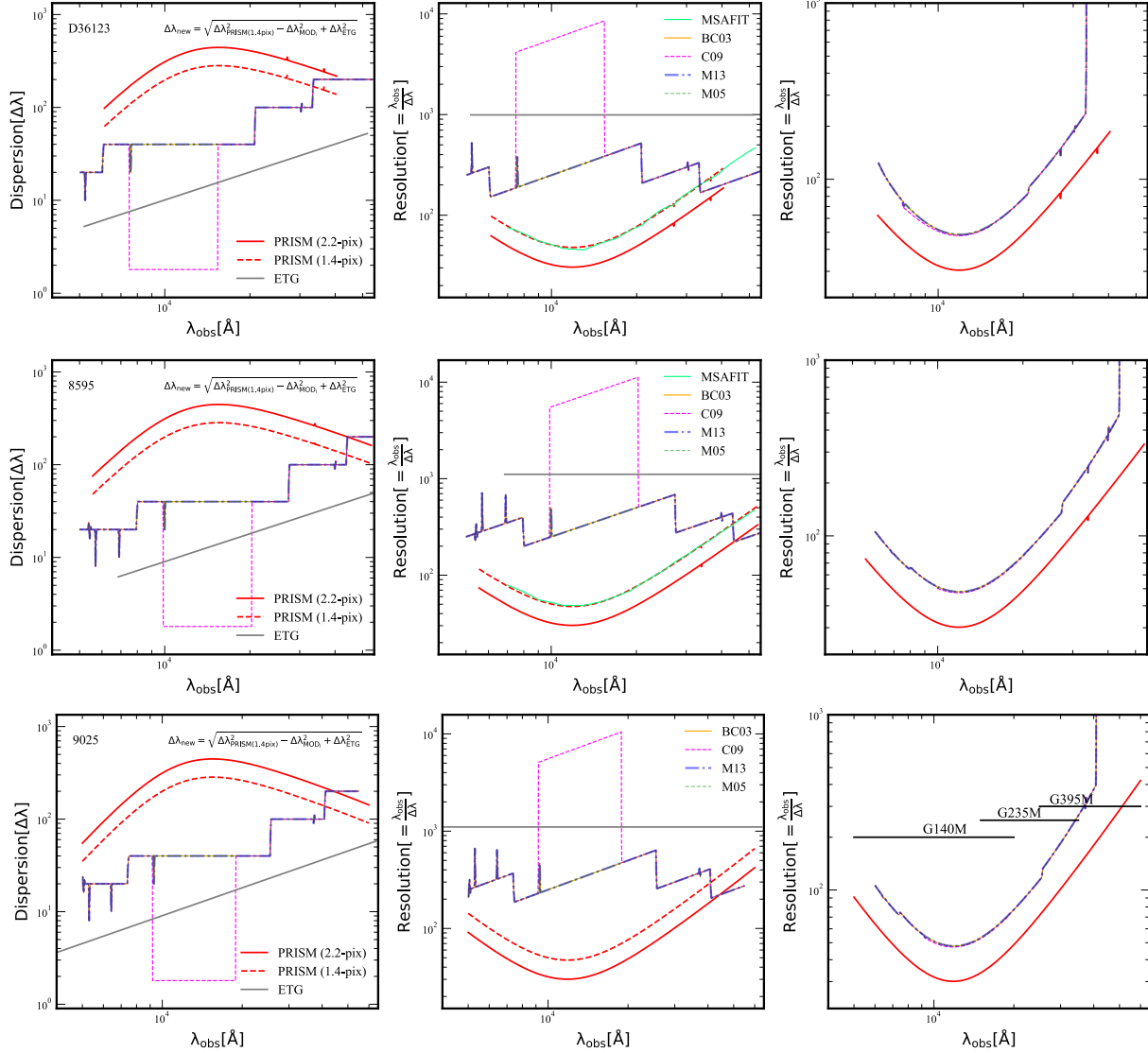


Figure 9: **Accounting for spectral resolution effects in matching observed spectra and spectral synthesis models.** The left panels display the dispersions $\Delta\lambda$ [Å], the middle panels present the corresponding resolutions, while the right panels show the effective resolution for convolving models to match that of the observed spectra. Instrumental resolutions for the PRISM based on 2.2-/1.4-pix elements in the shutter are in solid/dashed red lines. The instrumental resolution calculated by the MSAFIT code⁶⁷ based on actual galaxy sizes and shapes is shown in green for objects D36123 and 8595, except for object 9025 where the spectrum is resampled to the PRISM resolution. The model resolutions are in different color (BC03: orange; C09: magenta; M13: blue; M05: green). The intrinsic dispersion (converted to resolution) of the galaxies, based on local ETGs of the same stellar mass, are in gray.

Table 4: Parametric grid in D36123 spectral fit

Parameters [units]	Min	Max	Step
z	1.06	1.1	0.001
Age [Gyr]	0.1	3.5	0.1
	0.001, 0.004, 0.009, 0.05		
τ [Gyr]	0.1	1.0	0.1
	1.0	3.0	1.0
Av [mag]	0	2.1	0.1 (Calzetti)
	0.3	2.5	0.1 (BC03)
Z/Z_{\odot}	0.3	2.0	0.1 (C09)
	0.3	2.2	0.1 (M13)
	0.5	2.0	0.1 (M05)

2000¹³) and redward with the Aringer et al. (2009)⁷¹ synthetic carbon star spectral library. The spectra of the oxygen-rich TP-AGB stars are extrapolated with the latest version of the PHOENIX stellar spectral library (the BT-SETTL library). For the TP-AGB isochrones, there is no shift adopted in the $\log(L_{\text{bol}})$ vs. $\log(T_{\text{eff}})$. For crude understanding of the effect of TP-AGB stars in the NIR mass-to-light ratio we show 1 Gyr SSP models at solar metallicity from the different libraries, in Fig.12.

Data availability The JWST NIRSpec data are available from the Mikulski Archive for Space Telescope (MAST; <http://archive.stsci.edu>), under program IDs 1345 and 2750. The CEERS JWST imaging data are available from MAST under program ID 1345. Reduced NIRCam data products from the CEERS team are available at <https://ceers.github.io>. The HST imaging data are available from the CANDELS survey at <https://archive.stsci.edu/hlsp/candels>, and the NIR-Cam/Ks imaging data are published in the 3D-HST survey at <https://archive.stsci.edu/prepds/3d-hst/>. We publicly release in a digital form of the calibrated spectrum of D36123 to enable tuning of future generations of spectral synthesis models (upon acceptance of this paper).

Code availability The JWST NIRSpec data were reduced using the JWST Pipeline (version 1.8.5, reference mapping 1041 and 1029; <https://github.com/spacetelescope/jwst>). The MSAFIT software is available at <https://github.com/annadeg/jwst-msafit>. The `galfit` software is published at <https://users.obs.carnegiescience.edu/peng/work/galfit/galfit.html>.

Acknowledgements We thank Livia Origlia and Benne Holwerda for discussions. MD, PAH, SLF, JSK and CP acknowledge support from NASA through the STScI ERS award JWST-ERS-1345 and the JWST-GO-2750 award. CGG acknowledges support from CNES. CDE acknowledges funding from the MCIN/AEI (Spain) and the “NextGenerationEU”/PRTR (European Union) through the Juan de la Cierva-Formación program (FJC2021-047307-I). SL acknowledges the support by China Scholarship

Council (CSC). This work is supported by the National Natural Science Foundation of China (No. 12192222, 12192220 and 12121003). This work is based on observations with the NASA/ESA/CSA James Webb Space Telescope obtained from the Mikulski Archive for Space Telescopes at the STScI, which is operated by the Association of Universities for Research in Astronomy (AURA), Incorporated, under NASA contract NAS5-03127.

Author contributions SL and ED conceived this project, and selected and identified galaxies. SL led the analysis and together with ED, CM and MD wrote the manuscript. PAH and MD led the original observations and reduced the NIRSpec spectra. RG wrote the fitting code and with CDE helped with the spectral fitting procedures. All authors aided in the analysis and interpretation and contributed to the final manuscript.

Competing interests The authors declare that they have no competing financial interests.

1. Renzini, A. Energetics of stellar populations. *Ann. Phys.* **6**, 87–102 (1981). URL <https://doi.org/10.1051/anphys/198106060087>.
2. Maraston, C. Evolutionary synthesis of stellar populations: a modular tool. *Mon. Not. R. Astron. Soc.* **300**, 872–892 (1998).
3. Maraston, C. Evolutionary population synthesis: models, analysis of the ingredients and application to high-z galaxies. *Mon. Not. R. Astron. Soc.* **362**, 799–825 (2005).
4. Salaris, M., Weiss, A., Cassarà, L. P., Piovan, L. & Chiosi, C. Detailed AGB evolutionary models and near-infrared colours of intermediate-age stellar populations: tests on star clusters. *Astron. Astrophys.* **565**, A9 (2014).
5. Maraston, C. *et al.* Evidence for TP-AGB Stars in High-Redshift Galaxies, and Their Effect on Deriving Stellar Population Parameters. *Astrophys. J.* **652**, 85–96 (2006).
6. Tonini, C., Maraston, C., Devriendt, J., Thomas, D. & Silk, J. The impact of thermally pulsing asymptotic giant branch stars on hierarchical galaxy formation models. *Mon. Not. R. Astron. Soc.* **396**, L36–L40 (2009).
7. Bruzual, G. & Charlot, S. Stellar population synthesis at the resolution of 2003. *Mon. Not. R. Astron. Soc.* **344**, 1000–1028 (2003).
8. Marigo, P. *et al.* Evolution of asymptotic giant branch stars. II. Optical to far-infrared isochrones with improved TP-AGB models. *Astron. Astrophys.* **482**, 883–905 (2008).
9. Conroy, C., Gunn, J. E. & White, M. The Propagation of Uncertainties in Stellar Population Synthesis Modeling. I. The Relevance of Uncertain Aspects of Stellar Evolution and the Initial Mass Function to the Derived Physical Properties of Galaxies. *Astrophys. J.* **699**, 486–506 (2009).
10. Noël, N. E. D., Greggio, L., Renzini, A., Carollo, C. M. & Maraston, C. Calibrating Stellar Population Models with Magellanic Cloud Star Clusters. *Astrophys. J.* **772**, 58 (2013).

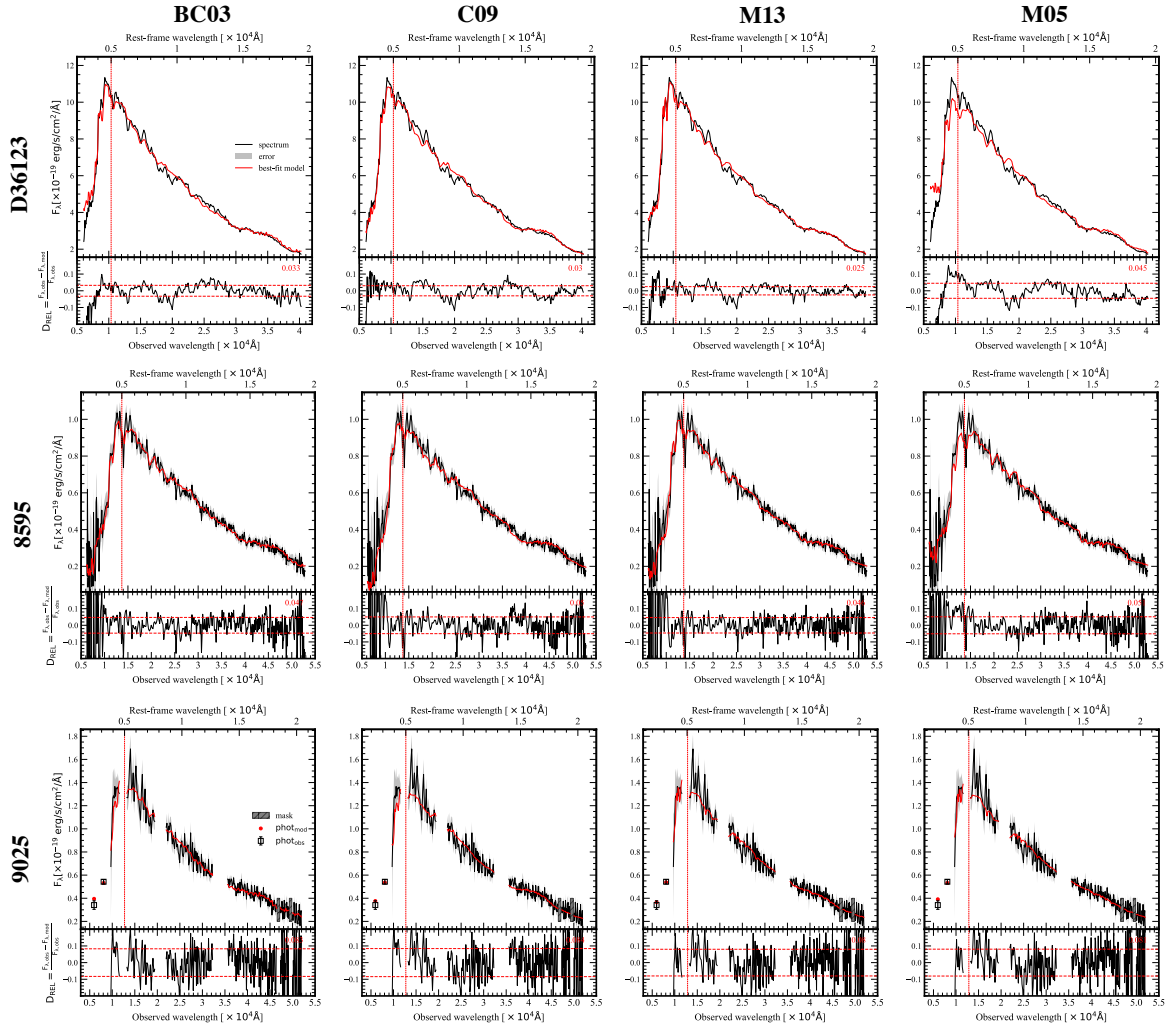


Figure 10: **Best-fit results and relative deviation.** From left to right, the best fits (top) and relative deviations (bottom) obtained by fitting BC03, C09, M13, and M05 models are shown. The panels from top to bottom present the results corresponding to D36123, 8595, and 9025 respectively. The red dashed lines are the SNR-weighted mean of the relative deviation, and the corresponding value is printed on the top-right of each bottom panels. Detector defects in the spectrum of object 9025 are masked by gray rectangles.

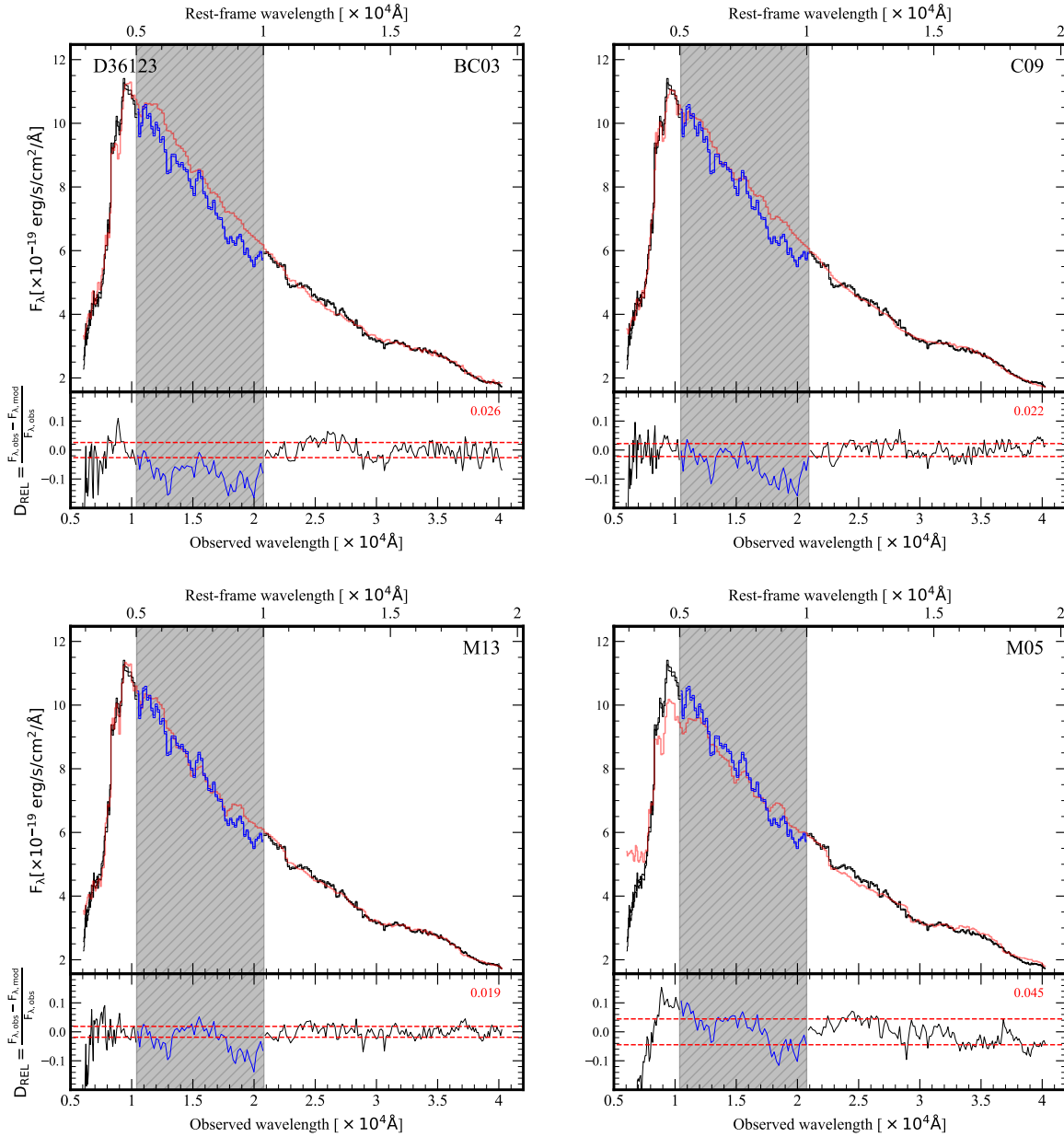


Figure 11: **Best-fit results and relative deviation of D36123, excluding the rest-frame 0.5–1 μm wavelength region.** Analogous to the previous figure. The excluded part in the spectral fit is shown in blue histograms, and covered by gray shaded region.

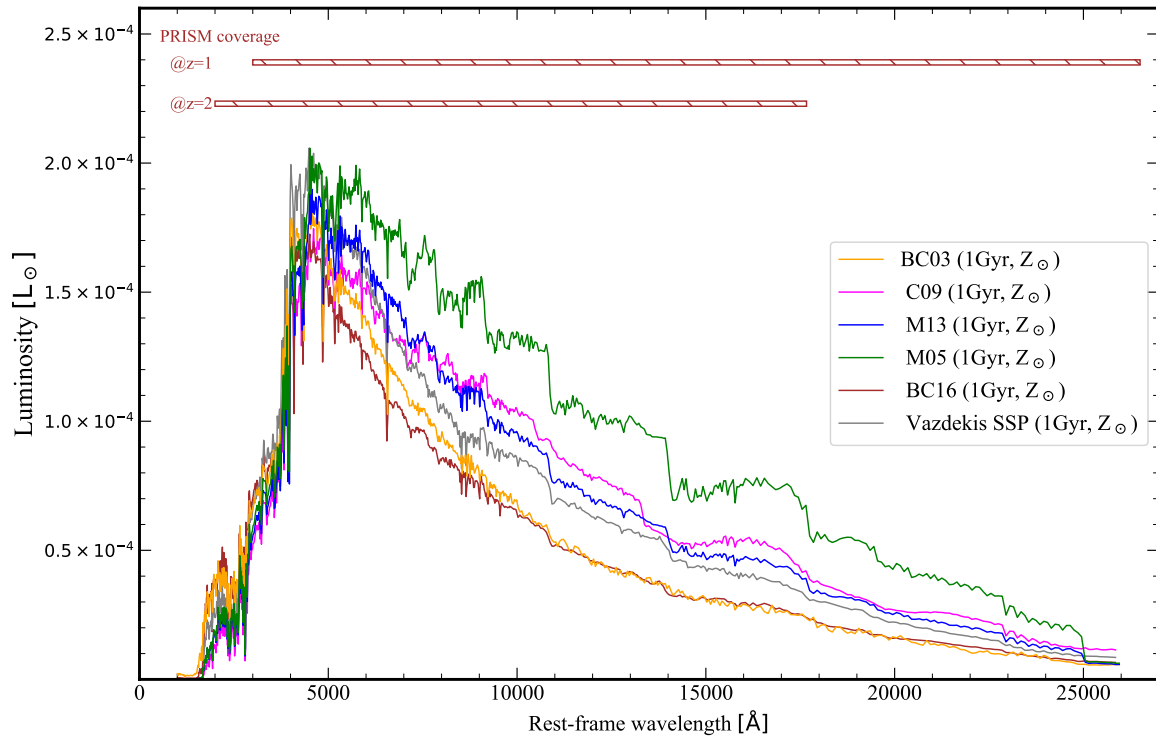


Figure 12: **The SEDs of four simple stellar population (SSP) models of $1 M_{\odot}$, 1Gyr and solar metallicity.** M05/M13 models include a larger contribution from cool C- and O-rich stars compared to the BC03/C09 models. The BC16 models is the 2016 version of the BC03 model. The Vazdekis SSP is constructed via isochrone synthesis, contains all phases but excludes the TP-AGB phase. The growing NIR output can be viewed as a gauge of decreasing mass-to-light (M/L) ratios. The rest-frame PRISM coverages at $z=1$ and $z=2$, respectively, are depicted at the top.

11. Pastorelli, G. *et al.* Constraining the thermally pulsing asymptotic giant branch phase with resolved stellar populations in the Large Magellanic Cloud. *Mon. Not. R. Astron. Soc.* **498**, 3283–3301 (2020).
12. Renzini, A. & Voli, M. Advanced Evolutionary Stages of Intermediate Mass Stars. I. Evolution of Surface Compositions. *Astron. Astrophys.* **94**, 175 (1981).
13. Lançon, A. & Wood, P. R. A library of 0.5 to 2.5 μm spectra of luminous cool stars. *Astron. Astrophys. Suppl.* **146**, 217–249 (2000).
14. Lançon, A. & Mouhcine, M. The modelling of intermediate-age stellar populations. II. Average spectra for upper AGB stars, and their use. *Astron. Astrophys.* **393**, 167–181 (2002).
15. Girardi, L., Bressan, A., Bertelli, G. & Chiosi, C. Evolutionary tracks and isochrones for low- and intermediate-mass stars: From 0.15 to 7 M_{sun} , and from $Z=0.0004$ to 0.03. *Astron. Astrophys. Suppl.* **141**, 371–383 (2000).
16. Kriek, M. *et al.* The Spectral Energy Distribution of Post-starburst Galaxies in the NEWFIRM Medium-band Survey: A Low Contribution from TP-AGB Stars. *Astrophys. J. Lett.* **722**, L64–L69 (2010).
17. Zibetti, S., Gallazzi, A., Charlot, S., Pierini, D. & Pasquali, A. Near-infrared spectroscopy of post-starburst galaxies: a limited impact of TP-AGB stars on galaxy spectral energy distributions. *Mon. Not. R. Astron. Soc.* **428**, 1479–1497 (2013).
18. Riffel, R. *et al.* The stellar spectral features of nearby galaxies in the near infrared: tracers of thermally pulsing asymptotic giant branch stars? *Mon. Not. R. Astron. Soc.* **450**, 3069–3079 (2015).
19. Capozzi, D. *et al.* Revisiting the role of the thermally pulsating asymptotic-giant-branch phase in high-redshift galaxies. *Mon. Not. R. Astron. Soc.* **456**, 790–830 (2016).
20. Martínez-García, E. E., Bruzual, G., González-Lópezlira, R. A. & Rodríguez-Merino, L. H. On the Thermally Pulsing Asymptotic Giant Branch Contribution to the Light of Nearby Disk Galaxies. *Astrophys. J.* **908**, 110 (2021).
21. Liu, S. & Luo, A. L. The Significance of Thermally Pulsing Asymptotic Giant Branch Stars in Post-starburst Galaxies. *Research in Astronomy and Astrophysics* **23**, 015017 (2023).
22. Stefanon, M. *et al.* CANDELS Multi-wavelength Catalogs: Source Identification and Photometry in the CANDELS Extended Groth Strip. *Astrophys. J. Suppl. Ser.* **229**, 32 (2017).
23. Grogin, N. A. *et al.* CANDELS: The Cosmic Assembly Near-infrared Deep Extragalactic Legacy Survey. *Astrophys. J. Suppl. Ser.* **197**, 35 (2011).
24. Koekemoer, A. M. *et al.* CANDELS: The Cosmic Assembly Near-infrared Deep Extragalactic Legacy Survey—The Hubble Space Telescope Observations, Imaging Data Products, and Mosaics. *Astrophys. J. Suppl. Ser.* **197**, 36 (2011).
25. Whitaker, K. E. *et al.* The NEWFIRM Medium-band Survey: Photometric Catalogs, Redshifts, and the Bimodal Color Distribution of Galaxies out to $z \sim 3$. *Astrophys. J.* **735**, 86 (2011).
26. Finkelstein, S. L. *et al.* CEERS Key Paper. I. An Early Look into the First 500 Myr of Galaxy Formation with JWST. *Astrophys. J. Lett.* **946**, L13 (2023).
27. Arrabal Haro, P. *et al.* Spectroscopic Confirmation of CEERS NIRCcam-selected Galaxies at $z = 8$ –10. *Astrophys. J. Lett.* **951**, L22 (2023).
28. Arrabal Haro, P. *et al.* Confirmation and refutation of very luminous galaxies in the early Universe. *Nature* **622**, 707–711 (2023).
29. Onodera, M. *et al.* The Ages, Metallicities, and Element Abundance Ratios of Massive Quenched Galaxies at $z \approx 1.6$. *Astrophys. J.* **808**, 161 (2015).
30. Lançon, A., Goldader, J. D., Leitherer, C. & González Delgado, R. M. Multiwavelength Study of the Starburst Galaxy NGC 7714. II. The Balance between Young, Intermediate-Age, and Old Stars. *Astrophys. J.* **552**, 150–167 (2001).
31. Habing, H. J. & Olofsson, H. *Asymptotic Giant Branch Stars* (2004).
32. Riffel, R., Pastoriza, M. G., Rodríguez-Ardila, A. & Maraston, C. The First Detection of Near-Infrared CN Bands in Active Galactic Nuclei: Signature of Star Formation. *Astrophys. J. Lett.* **659**, L103–L106 (2007).
33. Rayner, J. T., Cushing, M. C. & Vacca, W. D. The Infrared Telescope Facility (IRTF) Spectral Library: Cool Stars. *Astrophys. J. Suppl. Ser.* **185**, 289–432 (2009).
34. Faber, S. M., Friel, E. D., Burstein, D. & Gaskell, C. M. Old stellar populations. II. an analysis of K-giant spectra. *Astrophys. J. Suppl. Ser.* **57**, 711–741 (1985).
35. Thomas, D., Maraston, C., Bender, R. & Mendes de Oliveira, C. The Epochs of Early-Type Galaxy Formation as a Function of Environment. *Astrophys. J.* **621**, 673–694 (2005).
36. Ferraro, F. R., Origlia, L., Testa, V. & Maraston, C. Probing the Red Giant Branch Phase Transition: Near-Infrared Photometry of Six Intermediate-Age Large Magellanic Cloud Clusters. *Astrophys. J.* **608**, 772–780 (2004).
37. Vazdekis, A., Koleva, M., Ricciardelli, E., Röck, B. & Falcón-Barroso, J. UV-extended E-MILES stellar population models: young components in massive early-type galaxies. *Mon. Not. R. Astron. Soc.* **463**, 3409–3436 (2016).
38. Bruzual A., G. & Charlot, S. Spectral Evolution of Stellar Populations Using Isochrone Synthesis. *Astrophys. J.* **405**, 538 (1993).
39. Baldwin, C., McDermid, R. M., Kuntschner, H., Maraston, C. & Conroy, C. Comparison of stellar population model predictions using optical and infrared spectroscopy. *Mon. Not. R. Astron. Soc.* **473**, 4698–4721 (2018).

40. Dahmer-Hahn, L. G. *et al.* Probing evolutionary population synthesis models in the near infrared with early-type galaxies. *Mon. Not. R. Astron. Soc.* **476**, 4459–4480 (2018).
41. Eftekhari, E., La Barbera, F., Vazdekis, A., Allende Prieto, C. & Knowles, A. T. Strong CO absorption features in massive ETGs. *Mon. Not. R. Astron. Soc.* **512**, 378–400 (2022).
42. Riffel, R. *et al.* Erratum: Optical/NIR stellar absorption and emission-line indices from luminous infrared galaxies. *Mon. Not. R. Astron. Soc.* **486**, 5074–5074 (2019).
43. Conroy, C. & Gunn, J. E. The Propagation of Uncertainties in Stellar Population Synthesis Modeling. III. Model Calibration, Comparison, and Evaluation. *Astrophys. J.* **712**, 833–857 (2010).
44. Thomas, D., Maraston, C., Schawinski, K., Sarzi, M. & Silk, J. Environment and self-regulation in galaxy formation. *Mon. Not. R. Astron. Soc.* **404**, 1775–1789 (2010).
45. Lonoce, I. *et al.* Old age and supersolar metallicity in a massive $z \sim 1.4$ early-type galaxy from VLT/X-Shooter spectroscopy. *Mon. Not. R. Astron. Soc.* **454**, 3912–3919 (2015).
46. Kriek, M. *et al.* A massive, quiescent, population II galaxy at a redshift of 2.1. *Nature* **540**, 248–251 (2016).
47. Johansson, J., Thomas, D. & Maraston, C. Chemical element ratios of Sloan Digital Sky Survey early-type galaxies. *Mon. Not. R. Astron. Soc.* **421**, 1908–1926 (2012).
48. Worthey, G., Tang, B. & Serven, J. Individual Alpha Elements, C, N, and Ba in Early-type Galaxies. *Astrophys. J.* **783**, 20 (2014).
49. Conroy, C., Graves, G. J. & van Dokkum, P. G. Early-type Galaxy Archeology: Ages, Abundance Ratios, and Effective Temperatures from Full-spectrum Fitting. *Astrophys. J.* **780**, 33 (2014).
50. Parikh, T. *et al.* SDSS-IV MaNGA: the spatially resolved stellar initial mass function in ~ 400 early-type galaxies. *Mon. Not. R. Astron. Soc.* **477**, 3954–3982 (2018).
51. Worthey, G., Faber, S. M. & Gonzalez, J. J. Mg and Fe Absorption Features in Elliptical Galaxies. *Astrophys. J.* **398**, 69 (1992).
52. Thomas, D., Maraston, C. & Bender, R. Stellar population models of Lick indices with variable element abundance ratios. *Mon. Not. R. Astron. Soc.* **339**, 897–911 (2003).
53. Dell’Agli, F. *et al.* AGB stars in the SMC: evolution and dust properties based on Spitzer observations. *Mon. Not. R. Astron. Soc.* **454**, 4235–4249 (2015).
54. Kelson, D. D. & Holden, B. P. The Mid-infrared Luminosities of Normal Galaxies Over Cosmic Time. *Astrophys. J. Lett.* **713**, L28–L32 (2010).
55. Chabrier, G. Galactic Stellar and Substellar Initial Mass Function. *Publ. Astron. Soc. Pac.* **115**, 763–795 (2003).
56. Jakobsen, P. *et al.* The Near-Infrared Spectrograph (NIRSpec) on the James Webb Space Telescope. I. Overview of the instrument and its capabilities. *Astron. Astrophys.* **661**, A80 (2022).
57. Fujimoto, S. *et al.* CEERS Spectroscopic Confirmation of NIRCам-selected $z \gtrsim 8$ Galaxy Candidates with JWST/NIRSpec: Initial Characterization of Their Properties. *Astrophys. J. Lett.* **949**, L25 (2023).
58. Kocevski, D. D. *et al.* Hidden Little Monsters: Spectroscopic Identification of Low-mass, Broad-line AGNs at $z > 5$ with CEERS. *Astrophys. J. Lett.* **954**, L4 (2023).
59. Larson, R. L. *et al.* A CEERS Discovery of an Accreting Supermassive Black Hole 570 Myr after the Big Bang: Identifying a Progenitor of Massive $z \lesssim 6$ Quasars. *Astrophys. J. Lett.* **953**, L29 (2023).
60. Bushouse, H. *et al.* JWST Calibration Pipeline (2022).
61. Ferruit, P. *et al.* The Near-Infrared Spectrograph (NIRSpec) on the James Webb Space Telescope. II. Multi-object spectroscopy (MOS). *Astron. Astrophys.* **661**, A81 (2022).
62. Finkelstein, S. L. *et al.* A Long Time Ago in a Galaxy Far, Far Away: A Candidate $z \sim 12$ Galaxy in Early JWST CEERS Imaging. *Astrophys. J. Lett.* **940**, L55 (2022).
63. Peng, C. Y., Ho, L. C., Impey, C. D. & Rix, H.-W. Detailed Structural Decomposition of Galaxy Images. *Astron. J.* **124**, 266–293 (2002).
64. Peng, C. Y., Ho, L. C., Impey, C. D. & Rix, H.-W. Detailed Decomposition of Galaxy Images. II. Beyond Axisymmetric Models. *Astron. J.* **139**, 2097–2129 (2010).
65. Gómez-Guijarro, C. *et al.* JWST CEERS probes the role of stellar mass and morphology in obscuring galaxies. *Astron. Astrophys.* **677**, A34 (2023).
66. Bertin, E. Automated Morphometry with SExtractor and PSFEx. In Evans, I. N., Accomazzi, A., Mink, D. J. & Rots, A. H. (eds.) *Astronomical Data Analysis Software and Systems XX*, vol. 442 of *Astronomical Society of the Pacific Conference Series*, 435 (2011).
67. de Graaff, A. *et al.* Ionised gas kinematics and dynamical masses of *zrsim6* galaxies from JADES/NIRSpec high-resolution spectroscopy. *arXiv e-prints* arXiv:2308.09742 (2023).
68. Gobat, R. *et al.* The Early Early Type: Discovery of a Passive Galaxy at $z_{spec} \sim 3$. *Astrophys. J. Lett.* **759**, L44 (2012).
69. Calzetti, D. *et al.* The Dust Content and Opacity of Actively Star-forming Galaxies. *Astrophys. J.* **533**, 682–695 (2000).
70. Avni, Y. Energy spectra of X-ray clusters of galaxies. *Astrophys. J.* **210**, 642–646 (1976).
71. Aringer, B., Girardi, L., Nowotny, W., Marigo, P. & Lederer, M. T. Synthetic photometry for carbon rich giants. I. Hydrostatic dust-free models. *Astron. Astrophys.* **503**, 913–928 (2009).